Mon. Not. R. Astron. Soc. **306,** 575–591 (1999)

Superlarge-scale structure in *N*-body simulations

A. G. Doroshkevich,[1,2] V. Müller,[3] J. Retzlaff[3] and V. Turchaninov[2]

[1] *Theoretical Astrophysics Center, Juliane Maries Vej 30, DK-2100 Copenhagen Ø, Denmark*
[2] *Keldysh Institute of Applied Mathematics, Russian Academy of Sciences, 125047 Moscow, Russia*
[3] *Astrophysikalisches Institute Potsdam, An der Sternwarte 16, D-14482 Potsdam, Germany*

Accepted 1999 February 8. Received 1998 December 2; in original form 1998 June 11

ABSTRACT

The simulated matter distribution on large scales is studied using core-sampling, cluster analysis, inertia tensor analysis and minimal spanning tree techniques. Seven simulations in large boxes for five cosmological models with *COBE*-normalized CDM-like power spectra are studied. A wall-like superlarge-scale structure with parameters similar to the observed one is found for the OCDM and ΛCDM models with $\Omega_{\rm m}h = 0.2$–0.3. In these simulations, the rich structure elements with a typical value for the largest extension of $\sim(30-50)\,h^{-1}$ Mpc incorporate ∼40 per cent of matter with overdensity of about 10 above the mean. These rich elements are formed by the anisotropic non-linear compression of sheets with an original size of $\sim(15$–$25)\,h^{-1}$ Mpc. They surround low-density regions with a typical diameter $\sim(50$–$70)\,h^{-1}$ Mpc.

The statistical characteristics of these structures are found to be approximately consistent with observations and theoretical expectations. The cosmological models with higher matter density $\Omega_{\rm m} = 1$ in CDM with Harrison–Zeldovich or tilted power spectra cannot reproduce the characteristics of the observed galaxy distribution because of the very strong disruption of the rich structure elements. Another model with a broken scale-invariant initial power spectrum (BCDM) does not show enough matter concentration in the rich structure elements.

Key words: methods: numerical – cosmology: theory – dark matter – large-scale structure of Universe.

1 INTRODUCTION

The phenomenon of superlarge-scale structure (SLSS) was first observed as a rare peculiarity in the visible galaxy distribution, with extreme parameters. Examples of this include the Great Void (Kirshner et al. 1983), the Great Attractor (Dressler et al. 1987), the Great Wall (de Lapparent, Geller, & Huchra 1988; Ramella, Geller, & Huchra 1992), and the Pisces–Perseus supercluster (Giovanelli & Haynes 1993). Several nearby superclusters of galaxies were described by Oort (1983a,b). SLSS was also found in deep pencil-beam redshift surveys (Broadhurst et al. 1990; Willmer et al. 1994; Buryak, Doroshkevich & Fong 1994; Bellanger & de Lapparent 1995; Cohen et al. 1996) as rich galaxy clumps with typical separations in the range of 60–$120\,h^{-1}$ Mpc (h is the Hubble parameter in units of $100\,{\rm km\,s^{-1}\,Mpc^{-1}}$).

Recently the analyses of rich galaxy surveys with an effective depth $\sim(200-400)\,h^{-1}$ Mpc, such as the Durham/UKST Galaxy Redshift Survey (Ratcliffe et al. 1996) and the Las Campanas Redshift Survey (LCRS, Shectman et al. 1996), have established the existence of wall-like SLSS as a typical phenomenon in the visible galaxy distribution incorporating ∼40–50 per cent of galaxies (Doroshkevich et al. 1996, hereafter LCRS1; Doroshkevich et al. 1997b, hereafter LCRS2; 1998a; 1999). The wall-like SLSS consists of structure elements with a typical diameter $\sim(30$–$50)\,h^{-1}$ Mpc surrounding low-density regions (LDR) with a similar typical diameter $D_{\rm LDR} \sim (50$–$70)\,h^{-1}$ Mpc. Within the wall-like SLSS elements the observed galaxy distribution is also inhomogeneous (see e.g. fig. 5 of Ramella et al. 1992), and galaxies are concentrated in high-density clumps and filaments.

In LDR the galaxies are found to be concentrated within a random network of filaments. In distinction to typical wall-like superclusters, the galaxy distribution in LDR is predominantly one-dimensional with a mean separation of filaments ~ 10–$15\,h^{-1}$ Mpc (LCRS1), and we call this network large-scale structure (LSS). The LSS also incorporates ∼50 per cent of galaxies and is clearly seen in many redshift catalogues of galaxies (see e.g. de Lapparent et al. 1988). These results extend the range of investigated scales in the galaxy distribution up to $\sim 100\,h^{-1}$ Mpc.

While LSS was predicted by the non-linear theory of gravitational instability (Zel'dovich 1970), and was reproduced in simulations before its discovery in observations (see, for reference, Shandarin & Zel'dovich 1989), the observation of the rich and typically wall-like SLSS was quite unexpected. Thus, in simulations the representative SLSS was found only recently for a CDM model with low density and a cosmological constant (ΛCDM, Cole et al. 1997). This simulation demonstrates that for suitable

parameters of cosmological models the formation of the wall-like SLSS is compatible with the standard CDM power spectrum of Gaussian initial perturbations.

The formation and evolution of structure on all scales is described by an approximate theoretical model (Demiański & Doroshkevich 1998a,b) based on the Zel'dovich non-linear theory of gravitational instability (Zel'dovich 1970,1978; Shandarin & Zel'dovich 1989). The model shows that the SLSS formation can be related to matter infall into the large wells of the gravitational potential of the initial perturbations. This model connects the structure parameters with the main parameters of the underlying cosmological scenario and the initial power spectrum. It shows that the impact of large-scale perturbations is important throughout all evolutionary stages. In particular, the influence of these perturbations modulates the merging of smaller structure elements, promoting evolution within the SLSS elements and depressing it in LDR.

The simulations are able to take into account this interaction throughout all evolutionary stages and, therefore, are the most suitable way to study the properties and evolution of LSS and SLSS. This implies, however, that the simulations need to be performed in very large boxes both to provide us with reasonable statistics of the walls and, of particular importance, to describe correctly the large-scale part of the initial power spectrum of perturbations, responsible for the wall formation and the mutual interaction of small- and large-scale perturbations. In practice, this means that we need extreme parameters in the simulations. On the other hand, in order to compare various cosmological models a broad set of simulations has to be prepared.

Here results are presented from the analysis of simulations using five cosmological models. It is shown that the models with high matter density, $\Omega_{\rm m} \sim 1$, cannot reproduce adequately the observed properties of the large-scale matter distribution. The models with lower matter density, in particular the OCDM and ΛCDM models, seem to be more promising, since they can reproduce the general observed characteristics of both the LSS and the SLSS. In these models the rich structure elements, formed by a non-linear matter compression, contain a significant matter fraction, $f_{\rm rse} \sim 0.4$–0.5, which can be easily identified. A more detailed investigation of non-linear matter evolution on large scales is a further goal of this paper.

The small-scale matter clustering resulting in the destruction of structure elements restricts the class of cosmological models that are capable of reproducing the observed LSS and SLSS. The instability of a sheet-like matter distribution similar to the observed and simulated SLSS was considered (in the linear approximation) by Doroshkevich (1980) and Vishniac (1983), and it was recently simulated by Valinia et al. (1997).

Following our previous papers (LCRS1; LCRS2; Doroshkevich et al. 1997a) we concentrate on the geometrical properties of the matter distribution, in particular the proper sizes and spatial distribution of filaments and wall-like structure elements. The popular correlation analysis is not so useful at scales $> 10\,h^{-1}$ Mpc, discussed below, and other techniques provide us with better results. We employ the core-sampling approach introduced by Buryak et al. (1994), standard cluster analysis supplemented by the inertia tensor technique (Vishniac 1986; Babul & Starkman 1992), analysis of the variations of number of clusters versus linking length (NCLL method, LCRS2), and the minimal spanning tree (MST) technique (Barrow, Bhavsar & Sonoda 1985; van de Weygaert 1991). These methods were utilized recently for the investigation of structures in the LCRS (cf. LCRS1 and LCRS2) and Durham/UKST redshift surveys (Doroshkevich, Fong & Makarova 1999). These results will be used for comparison with the structure parameters derived from simulations. The different methods are complementary to each other, and, thus, they allow us to characterize the simulated matter distribution in different important aspects.

The observed distribution of galaxies and the simulated distribution of the dark matter (DM) cannot be identical, as the galaxy formation is sensitive to additional factors (e.g. to the reheating) and, moreover, galaxies probably mark only the highest peaks of density perturbations. This means that some parameters of DM structure elements such as their overdensity and proper sizes can differ from those found in observational catalogues. The comparative analysis performed for one simulation (Doroshkevich et al. 1998a) confirms that in some respect the spatial distributions of DM and 'galaxies' are different. A more detailed comparison of the observed and simulated matter distribution implies an identification of 'galaxies' in the simulated DM distribution. This means that a certain bias model needs to be utilized (see, e.g., discussions in Sahni & Coles 1995 and Cole et al. 1998). Both problems are, however, equally important, and the distributions of both the galaxies and the DM must be studied.

This paper is organized as follows. The simulations and the analysis techniques utilized are briefly described in Sections 2 and 3. In Section 4 the general characteristics of the considered simulations are discussed that allow us to discriminate roughly between the cosmological models and to select the most realistic ones for a more detailed investigation. Our main results are presented in Sections 5 and 6. Section 7 is devoted to the comparison of the DM distribution with theoretical expectations, and in Section 8 we discuss mock galaxy catalogues using some simple bias models. The conclusion and a discussion can be found in Section 9.

2 SIMULATIONS

We used five cosmological models as a basis for our analysis. The *COBE*-normalized SCDM model is taken as a reference model despite its difficulties in explaining already standard measures of galaxy clustering such as the power spectrum and the correlation function of galaxies and galaxy clusters (cf. e.g. Ostriker, 1993). Alternative models with $\Omega_{\rm m} = 1$ include modifications of the primordial power spectrum, in particular by introducing a tilt $\propto k^{0.9}$ of the power spectrum (TCDM), or a break at a certain scale (BCDM). Both are inflation-motivated, using either an exponential inflation potential (Lucchin & Matarrese 1985), or a double inflation scenario (Gottlöber, Müller & Starobinsky 1991). The BCDM is specified by two parameters, the location of the break at $k_{\rm break}^{-1} = 1.5\,h^{-1}$ Mpc, and the relative power on both sides of the break, $\Delta = 3$. These parameters were originally chosen to obtain optimal linear fits to the various large-scale structure observations (Gottlöber, Mücket & Starobinsky 1994), and later tested against *N*-body simulations (Amendola et al. 1995; Kates et al. 1995; Ghigna et al. 1996; Retzlaff et al. 1998). Both TCDM and BCDM models seemed to be promising since they have reduced power at galactic scales with respect to the *COBE*-normalized SCDM model.

Furthermore, two models are studied which are based on the wide range of observations pointing to a lower matter density in the Universe. First, we study an OCDM model with $\Omega_{\rm m} = 0.5$ violating the inflationary paradigm of a spatially flat universe. Secondly, we take a model with a cosmological constant, which has $\Omega_{\rm m} = 0.35$ and a vacuum energy leading again to a spatially flat universe. This ΛCDM model bears some advantage in alleviating the tight age

Table 1. Parameters of the simulations. Ω_m is the matter density, h is the dimensionless Hubble constant, L_{box} is the box size in h^{-1} Mpc, N_p and N_{cell} are the particle and cell numbers, σ_8 is the mass variance for the linear spectrum at the scale $8\,h^{-1}$ Mpc, σ_{vel} is the variance of the linear particle velocity in km s^{-1}.

model	Ω_m	h	L_{box}	N_p	N_{cell}	σ_8	σ_{vel}
SCDM1	1	0.5	500	300^3	600^3	1.05	1157
SCDM2	1	0.5	400	256^3	512^3	1.12	1127
TCDM	1	0.5	500	300^3	600^3	1.25	1293
BCDM	1	0.5	500	300^3	600^3	0.60	714
OCDM	0.5	0.6	500	300^3	600^3	0.74	550
ΛCDM1	0.35	0.7	500	300^3	600^3	1.12	913
ΛCDM2	0.35	0.7	400	256^3	512^3	1.30	873

constraint of the universe. For all models the standard parametrization of the CDM transfer function of Bardeen et al. (1986, hereafter BBKS) was used. In Table 1 the main parameters of the simulations are listed, including the matter density Ω_m, the dimensionless Hubble constant h, the box size L_{box}, the particle number N_p and the cell number N_{cell}. Two models (SCDM and ΛCDM) were simulated with different resolutions and with slightly different initial amplitudes.

The power spectra were normalized according to the two-year *COBE* measurements following Bunn, Scott & White (1995) (SCDM1, TCDM, BCDM, and ΛCDM1), or to the four-year data according to the description of Bunn & White (1997) (SCDM2, OCDM, ΛCDM2), in both cases assuming pure adiabatic perturbations and a baryon content of $\Omega_b h^2 = 2\times10^{-2}$ as predicted by big bang nucleosynthesis (see, e.g., Schramm 1998). Our later discussion will show that neither the smaller amplitude of the four-year normalization nor the contribution of gravitational waves and/or other inhomogeneities to the *COBE* signal influence significantly the main conclusions. The amplitude of perturbations is characterized by the mass variance for the linear spectrum at the scale $8\,h^{-1}$ Mpc, σ_8, and the three-dimensional velocity dispersion, σ_{vel}, gained from all dark matter particles in the simulation.

The simulations were run in boxes of comoving size $L_{box} = 500\,h^{-1}$ Mpc and $L_{box} = 400\,h^{-1}$ Mpc, respectively, to provide good statistics of perturbations in the range of wavenumbers $k^{-1} \sim (10\text{–}30)\,h^{-1}$ Mpc responsible for the SLSS formation and, therefore, to improve the statistical characteristics of SLSS elements and the description of the interaction of small- and large-scale perturbations. For such boxes the formation of the majority of structure elements is described by higher harmonics of the primordial density waves, with $l \geq 8\text{–}10$. We use the particle mesh (PM) code, described in more detail in Kates et al. (1995) and Retzlaff et al. (1998), with $N_p = 300^3$ or 256^3 particles in $N_{cell} = 600^3$ or 512^3 grid cells, respectively. These parameters provide a resolution $\sim 0.9\,h^{-1}$ Mpc and a mass resolution $\sim 1\text{–}3\times10^{11}\,M_\odot$.

Most statistics can be calculated only for subsamples of the huge data sets. Therefore, we mostly used slices of thickness $50\,h^{-1}$ Mpc of the simulation box, which are about 10 per cent of the complete volume. Even this volume provides us with a reasonable representation of the SLSS elements. This high stability of structure parameters is a direct consequence of the large box size used. To test the reliability, we repeated the analysis for different slices and constructed some statistics for the full volume taking the ΛCDM1 model. The main difference between the analysis of the full sample and slices is a variations of the mean velocity dispersion of clusters by 5–7 per cent. Similar differences are characteristic of different realizations of the same cosmological model (SCDM1 versus SCDM2, ΛCDM1 versus ΛCDM2). Below we give the basic results for the larger simulations only; they are denoted as SCDM and ΛCDM.

The comparison of simulated and observed parameters of the SLSS has to be done in the redshift space while the theoretical predictions are usually made in the comoving space. Hence, our analysis was performed twice. In the case of redshift space, we added an apparent displacement corresponding to the peculiar velocity of the particles along one axis divided by the Hubble constant. The comparison of results from real and redshift space allows us to establish the influence of the velocity dispersion on the final estimates.

Fig. 1 shows a wedge diagram of the simulated matter distribution in redshift space for the ΛCDM model at redshifts $z = 0$. To each particle we assigned a luminosity chosen at random from a

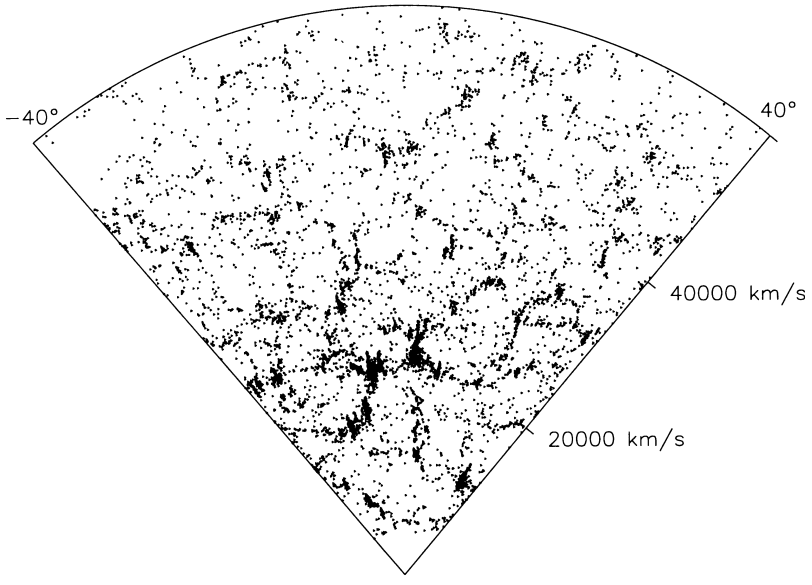

Figure 1. Simulated point distribution in redshift space for ΛCDM model at redshift $z = 0$.

Schechter luminosity function typical for the LCRS galaxies (Lin et al. 1996). We projected the particles into a wedge of angular extension $80^\circ \times 1.5^\circ$, and we kept simulated galaxies in the magnitude range $14 < m < 18$, about the range of the LCRS. The mock sample contains about 7500 galaxies. The figure illustrates that the overdense regions form almost a percolating system, with huge structured systems between radial velocities of 10 000–40 000 km s^{-1}. A sparse filamentary matter distribution occupies the low-density regions.

3 CORE-SAMPLING, CLUSTER ANALYSIS, AND MINIMAL SPANNING TREE TECHNIQUES

In this paper we are interested in the investigation of large-scale structure, and specific methods are to be used in order to characterize the simulated matter distribution. These methods are not so popular as, for example, the correlation analysis, but they are well defined and allow us to characterize the matter distribution on large scales comparable with observations and with the scales predicted by theoretical considerations.

3.1 Core-sampling approach

The core-sampling method proposed by Buryak et al. (1994) was described in detail in LCRS1 and tested with Voronoi tesselations by Doroshkevich, Gottlöber & Madsen (1997c). It allows us to discriminate between filamentary and sheet-like structure elements and to find two quantitative characteristics of the structure, namely the surface density of filaments, σ_f, that is the mean number of filaments crossing a randomly oriented unit area (i.e. $1\,h^{-2}\,\mathrm{Mpc}^2$), and the linear density of sheets, σ_s, that is the number of sheets crossing the unit length (i.e. $1\,h^{-1}\,\mathrm{Mpc}$) of a random straight line. These parameters are equivalent to the mean separation between sheet-like structure elements, D_s, and filaments, D_f:

$$D_s = 1/\sigma_s, \qquad D_f = \sigma_f^{-1/2}, \tag{3.1}$$

i.e. these lengths represent the mean free path between sheet-like and filamentary structure elements.

The core-sampling method also allows us to determine the masses and velocities of structure elements that intersect a sampling core, i.e. it provides the surface mass density and dynamical characteristics of structure elements. These parameters are used for the comparison with theoretical expectations.

3.2 Minimal spanning tree technique

The minimal spanning tree (MST) is a *unique network* associated with a given point sample and connects all points of the sample to a *tree* in a special and unique manner. Some definitions and capabilities of this approach are described by Barrow, Bhavsar & Sonoda (1985) and van de Weygaert (1991). Here we will restrict our investigation to the analysis of the *frequency distribution of the MST edge lengths* $W_{MST}(l)$ (the FDMST method). The potential of the MST approach is not exhausted by this application. It allows us to characterize, in particular, the morphology of structure elements and the typical size of the structure network.

At large distances any correlations between the particle positions are small, and it is expected that the edge length distribution $W_{MST}(l)$ is similar to that of a Poisson distribution. For filaments, however, this distribution will be dominated by a Poisson distribution with one-dimensional support (1D), whereas for sheet-like elements a nearly two-dimensional (2D) random point distribution is typical. This means that the function $W_{MST}(l)$ can be used to characterize statistically the dominant point distribution in the sample. To do this, the FDMST can be fitted to the six-parameter function

$$W_{MST}(x) = -W_0 \frac{\mathrm{d}F_f}{\mathrm{d}x}\, \mathrm{e}^{-F_f(x)}, \quad x = l/\langle l_{MST}\rangle, \tag{3.2}$$

$$F_f(x) = (\beta_1 x^{p_1} + \beta_2 x^{p_2})^{p_3},$$

$$p(x) = \frac{x}{F_f}\frac{\mathrm{d}F_f}{\mathrm{d}x} = p_3 \frac{p_1\beta_1 x^{p_1} + p_2\beta_2 x^{p_2}}{\beta_1 x^{p_1} + \beta_2 x^{p_2}},$$

where l and $\langle l_{MST}\rangle$ are the edge lengths and the mean edge length of the tree, and W_0 provides the normalization of the FDMST. The function F represents a power law both for small and large x, but it allows a continuous variation of the power index $p(x)$ with the edge lengths x.

Here we are mainly interested in the power index $p(x)$ for the larger x that characterizes the underlying geometry of the point distribution on large scales. Poisson point distributions with 1D and 2D support are characterized by the power indices $p = 1$ and 2, respectively. Therefore, the asymptote of the function $p(x)$ at large x characterizes the geometry of the structure elements, and it can be compared with similar parameters recently found for the observed galaxy distribution (LCRS2). This approach was tested with the simulations of 1D, 2D and 3D Poissonian-like point distributions.

3.3 Cluster analysis and variations of the number of clusters versus linking length – the NCLL method

The standard cluster analysis (friend-of-friends method) is used widely in numerical simulations and is well known (see, e.g. Sahni & Coles 1995). Here we employ it, first of all, in order to define the structure elements for a more detailed investigation of their properties. The cluster analysis can also be used for the description of the matter distribution on large scales. The function $W_{MST}(l)$ is closely connected with the number of clusters $N_{cl}^{(t)}(r_{link})$ because

$$N_{cl}^{(t)}(r_{link}) = N_p \int_{r_{link}}^{\infty} W_{MST}(l)\mathrm{d}l, \tag{3.3}$$

where N_p is the number of points in the sample under investigation. Therefore, the FDMST and NCLL approaches are similar in many respects.

We use a five-parameter fit of the cluster number versus linking length relations, $N_{cl}^{(t)}(r_{link})$:

$$N_{cl}(b) = N_p\, \mathrm{e}^{-F_f(b)}, \quad b = \left(\frac{4\pi}{3} n_p r_{link}^3\right)^{1/3}. \tag{3.4}$$

Here $F_f(b)$ is defined by (3.2), b is the dimensionless linking length, $\beta_1, \beta_2, p_1, p_2$ and p_3 are dimensionless fit parameters, and n_p is the 3D number density of points.

Here we are mainly interested in the variation of the power index $p(b)$ at large b. This method is complementary to the FDMST analysis, and it allows us to get an independent fit to the power index $p(b)$ at large b.

The NCLL method can also be extended, and, for the more detailed characteristics of the matter distribution, the variation of single particles, doublets, triplets and other clusters versus linking length can be considered as well. In this paper, we consider only the total number of clusters $N_{cl}^{(t)}(r_{link})$ for the comparison with results obtained with the FDMST.

Table 2. Parameters of rich structure elements in comoving (cm) and redshift (rs) space. $r_{\rm link}$, b are the threshold linking lengths, $b_{\rm perc}$ characterizes (approximate) percolation, $N_{\rm rse}$, $f_{\rm rse}$ and $\delta_{\rm rse}$ are the number and fraction of accumulated particles and mean overdensity, σ_u is the dispersion of velocity of RSE and σ_1,σ_2 and σ_3 are the velocity dispersion of matter within the structure elements along the three principal axes of their inertia tensor.

model	z	$r_{\rm link}$ h^{-1} Mpc	b^3	$b^3_{\rm perc}$	$N_{\rm rse}$	$f_{\rm rse}$	$\delta_{\rm rse}$	σ_u km s^{-1}	σ_1 km s^{-1}	σ_2 km s^{-1}	σ_3 km s^{-1}
SCDM-cm	0	0.75	0.38	2.22	1370	0.46	43.1	670	690	670	590
SCDM-rs	0	0.75	0.38	1.95	1134	0.45	10.2	610	716	743	703
OCDM-cm	0	0.95	0.77	1.39	474	0.39	4.0	416	333	341	343
OCDM-rs	0	0.95	0.77	1.45	469	0.44	3.8	400	325	340	344
ΛCDM-cm	0	1.	0.90	1.52	752	0.42	38.1	596	610	582	514
ΛCDM-rs	0	1.	0.90	1.30	697	0.45	14.1	548	565	590	530
ΛCDM-cm	1	1.	0.90	1.37	561	0.24	12.1	496	510	527	500
ΛCDM-rs	1	1.	0.90	1.44	599	0.28	10.1	458	473	512	497

3.4 Inertia tensor method

The sizes of structure elements can be found with the inertia tensor method (Vishniac 1986; Babul & Starkman 1992). For each cluster the inertia tensor I_{ij} is expressed as

$$I_{ij} = \frac{5}{N_{\rm mem}} \sum_{N_{\rm mem}} (q_i - q_i^{(0)})(q_j - q_j^{(0)}), \tag{3.5}$$

where q_i and $q_i^{(0)}$ are the coordinates of the particles and of the centre of mass of the cluster, respectively, and $N_{\rm mem}$ is the number of cluster members. The conventional normalization 5 has been taken to be consistent with a homogeneous ellipsoid. Hence, the principal values of the tensor I_{ij}, namely the length (diameter), L, the width, w, and the thickness, t ($L \geq w \geq t$), give us objective estimates of the cluster size and of the volume, V, and of the mean overdensity of cluster, δ

$$V = \frac{\pi}{6} Lwt, \quad \delta = \frac{N_{\rm mem}}{n_{\rm p} V} \ . \tag{3.6}$$

where $N_{\rm mem}$ is the number of points in the cluster.

This raw estimate is clearly of limited accuracy, but it is easy to calculate. The reliability of this estimate is high for compact regular clusters, and in general it depends on the cluster shape, in particular on its lumpiness (see, e.g., Sathyaprakash et al. 1998). We found from the simulations, that for large linking lengths, clusters are very lumpy in their outer regions. Then the ellipsoidal approximation leads to an artificial growth of the width and the thickness of the clusters. However, the cluster diameter L provides a stable characteristic of the cluster size.

4 RICH STRUCTURE ELEMENTS IN SIMULATIONS

The cluster analysis shows that rich structure elements (RSE) are usually represented by rather compact wall-like objects, and our methods give us more reliable information about their properties, some of which can be directly connected with the parameters of the cosmological model (see discussion in Section 7). In contrast, the discrimination and identification of poor structure elements is always difficult, as in the observed galaxy distribution they usually represent a filamentary component in a random network. This means that the identification and statistical description of such elements is often uncertain as their shapes are entangled due to many irregular branches.

Because of this, in this paper we mainly give our attention to the RSE. Some statistical parameters of the filamentary component have nonetheless been found. They are discussed below.

4.1 Identification of structure elements in simulations

The large size of the computation box allows us to obtain a representative set of large clusters which can be associated with the observed RSE. The clusters were found for different richness thresholds $N_{\rm thr}$, and for varying linking lengths $r_{\rm link}$. The linking length is directly connected with the density threshold bounding structure elements, $n_{\rm thr}$. Indeed, no particles of a cluster are separated from the neighbour by more than the distance $r_{\rm link}$, therefore a lower limit to the cluster density is

$$n_{\rm thr} \geq n_{\rm p} b^{-3}, \tag{4.1}$$

where b is given by (3.4).

For more interesting models the parameters $N_{\rm thr}$ and b, used for the identification of structure elements, as well as the number of identified structure elements, $N_{\rm rse}$, are listed in Table 2. We also give the value $b_{\rm perc}$ which corresponds to the linking length when the largest cluster of the sample accumulates ∼(25–30) per cent of the points. This is similar to, but not the exact percolation threshold (Klypin & Shandarin 1992). The smooth shape of FDMST (no break or cut-offs, see the discussion in Section 6.6) shows that in the simulated matter distribution, even for large b a significant fraction of points is not accumulated by the largest cluster. Nevertheless, the fast growth of the largest cluster distorts the cluster properties, therefore smaller linking lengths must be used to obtain the typical characteristics of rich structure elements.

A few parameters for the RSE are applied to discriminate between cosmological models, to select the most realistic models for a detailed analysis, and to find a reasonable range of the threshold for the discrimination between RSE and LDR. These parameters, also listed in Table 2, are the fraction of matter accumulated by such structure elements, $f_{\rm rse}$, the overdensity $\delta_{\rm rse}$ given by (3.6), the velocity dispersion of these structure elements, σ_u, and the velocity dispersion of matter within the structure elements along the three principal axes of their inertia tensor, σ_1, σ_2, σ_3. The overdensity, the velocity dispersion of the clusters and the inner velocity dispersion were averaged over all clusters in the sample within the range of richness under consideration. Each cluster was weighted by the number of cluster members, $N_{\rm mem}$, as this provides parameters typical for the majority of considered points. These characteristics are sensitive to $\Omega_{\rm m}$ and h, and to the

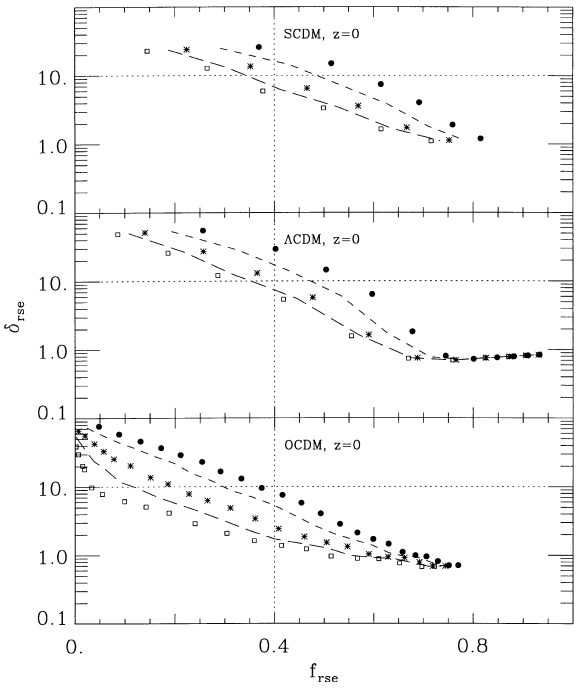

Figure 2. Overdensity $\delta_{\rm rse}$ in redshift space versus matter fraction concentrated within RSE, $f_{\rm rse}$, for five richness thresholds: $N_{\rm thr} = 100$ (dots), $N_{\rm thr} = 200$ (dashed line), $N_{\rm thr} = 300$ (stars), $N_{\rm thr} = 500$ (long-dashed line), $N_{\rm thr} = 1000$ (open squares). Dotted lines show the observed parameters of RSE.

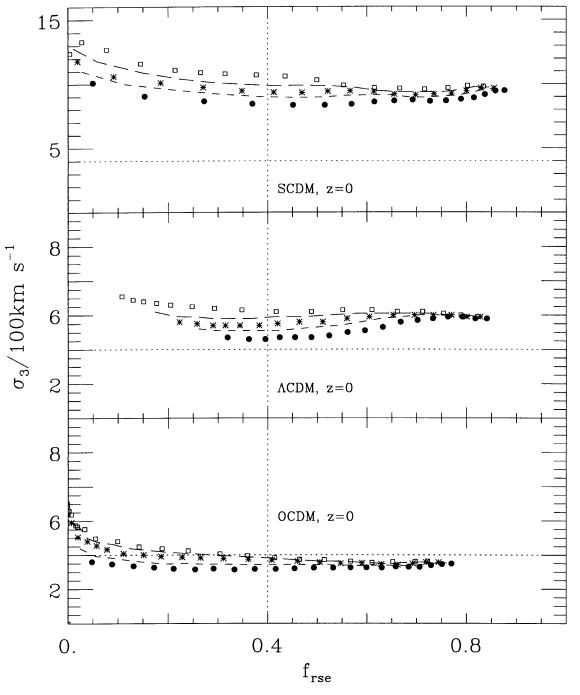

Figure 3. Velocity dispersion σ_3 in redshift space versus matter fraction concentrated within RSE, $f_{\rm rse}$, for the same five richness thresholds. Dotted lines show the observed parameters of RSE.

amplitude and the shape of power spectrum. They are found for all simulations. The overdensity and the component of the inner velocity dispersion along the axis with the smallest component of the inertia tensor, σ_3, are plotted in Figs 2 and 3 for SCDM, OCDM and ΛCDM models.

4.2 Overdensity and velocity dispersions of rich structure elements

The simulated characteristics of the RSE must be compared with the observed parameters. The velocity dispersion within wall-like structure elements was roughly estimated by Oort (1983a) to be $\sigma_v^{\rm obs} \sim 350$–$400\,{\rm km\,s^{-1}}$. An estimate of the bulk velocity $\sigma_u^{\rm obs} \sim 400\,{\rm km\,s^{-1}}$ can be taken from Dekel (1997). The fraction of galaxies accumulated by the RSE, $f_{\rm rse}$, and the corresponding overdensity, $\delta_{\rm rse}$, were estimated for the LCRS as $f_{\rm rse} \sim 0.4$–0.5 and $\delta_{\rm rse} \sim 10$ (LCRS1 and LCRS2). The spatial distribution of RSE can be characterized by the mean separation of RSE along a random straight line, which was found as $\sim(50$–$60)\,h^{-1}$ Mpc in the LCRS. Using these estimates, we can also find an approximate demarcation between RSE and LDR.

The analysis shows that the mean velocity of the clusters $\langle u\rangle$ is negligible in comparison with the velocity dispersion σ_u. This dispersion depends only weakly on the cluster richness, but it is sensitive to parameters of the cosmological model. Because of the vortex-free character of the initial velocity field the velocity u measures the random variation of the gravitational potential over the cluster and, therefore, the value σ_u is approximately proportional to the amplitude of initial perturbations given by the mean velocity dispersion, $\sigma_{\rm vel}$, listed in Table 1. Theoretical considerations (Demiański & Doroshkevich 1999b) describe this connection quantitatively (see also the discussion in Section 7). It can be expected that σ_u is slightly smaller in the MDM model where the fraction of hot DM particles makes the potential distribution more smooth. For the SCDM and TCDM models, the dispersions σ_u exceed the observed value by about a factor of 2, and by a factor of about 1.5 for ΛCDM model. For the OCDM and BCDM models, the simulated and observed velocity dispersions are in general consistent.

The mean overdensity and the inner velocity dispersion, σ_3, along the shorter cluster axis are very sensitive both to the cosmological model and to the subsample of clusters under investigation. For the most realistic models, they allow us to estimate a suitable range for the linking length, $r_{\rm link}$, and the threshold richness of clusters, $N_{\rm thr}$. For three models the overdensity, $\delta_{\rm rse}$, and the inner velocity dispersion, σ_3, are plotted in Figs 2 and 3 versus the matter fraction of the clusters, using five richness thresholds, $N_{\rm thr}$. In order to compare the parameters of the clusters with observations, the analysis has been performed in redshift space. The observed estimates of overdensity, galaxy concentration and velocity dispersion along the shorter principal axis of RSE, σ_3, are plotted in Figs 2 and 3 as well.

The simulated values of the velocity dispersion σ_3 exceed the theoretical expectations (Demiański & Doroshkevich 1999b) due to the wall disruption and the formation of high-density clumps. This is clearly seen from the isotropy of dispersion listed in Table 2 (we always have $\sigma_1 \sim \sigma_2 \sim \sigma_3$). The rate of this disruption depends on the degree of matter compression and, therefore, on the mean overdensity of the clusters.

The simulations with $\Omega_{\rm m} = 1$ (SCDM, TCDM and BCDM models) cannot reproduce the main observed characteristics of the RSE over the range of considered richness thresholds $100 < N_{\rm thr} < 1000$ and over a reasonable range of linking lengths. For the SCDM and TCDM models, a reasonable matter concentration is connected with a very large velocity dispersion. Therefore, even moderate changes in the power spectrum normalization of these models cannot improve the parameters of the rich clusters. For the BCDM model, a reasonable velocity dispersion is accompanied

by a very small matter concentration within the RSE. For this model a large bias between the galaxies and the dark matter distribution (a large factor ~2–3 is required) could, in principle, reduce this disagreement. The same effect can also be reached by an increase of the amplitude of the power spectrum by a factor of about 2 in comparison with the normalization used. Thus, already the first step of our analysis shows that probably models with $\Omega_m = 1$ cannot be considered as realistic.

Models with a smaller matter density $\Omega_m = 0.5$ (OCDM) and $\Omega_m = 0.35$ (ΛCDM) show better results. For the ΛCDM simulation reasonable structure parameters are found for $b^3 = 0.90$ and $N_{thr} = 200$. Some excess in the velocity dispersion σ_u and in σ_1, σ_2 and σ_3 (a factor of about 1.5) points to the over-evolution of this model. Better results can be reached by the variation of the DM composition and/or for smaller values of the cosmological parameters Ω_m and h. For the simulated OCDM model, all parameters of RSE at $b^3 = 0.77$ and $N_{thr} = 200$ are consistent with the observed ones in the range of our precision. A deficit in the overdensity ($\delta_{rse} \sim 4$) is within the range of a possible large-scale bias, i.e. a higher concentration of luminous matter (galaxies) in rich structure elements in comparison with the concentration of DM (see Section 8).

The considered low-density models are the most promising for a detailed investigation. In these models the *COBE* normalization is also consistent with the observed characteristics of rich clusters of galaxy (cf., e.g. Cole et al. 1997; Bahcall & Fan 1998). The curves in Figs 2 and 3 allow us to establish a rough boundary between the RSE and LDR, both in terms of the variables N_{thr} and r_{link} (or b), and in terms of physical variables f_{rse} and $\delta_{rse} = \langle n_{rse}\rangle/\langle n_p\rangle$. Furthermore, detailed investigation of RSE and LDR allow us to test for and to correct this demarcation.

A significant redshift dependence of the main parameters of RSE is found for ΛCDM models at $0 \le z \le 3$. Thus, already at $z = 1$ a smaller matter concentration is found, and at $z = 3$ the matter fraction in RSE, $f_{rse} \sim 0.03$–0.05, is negligible. This means that for these models the RSE are sensitive indicators of the initial amplitude of perturbations.

5 MEAN SEPARATION OF FILAMENTARY AND SHEET-LIKE COMPONENTS IN THE SCDM, OCDM AND ΛCDM MODELS

In this section, properties of simulated structures are examined with the core-sampling method. This method allows us to find the mean separations between filamentary and sheet-like structure elements, respectively. The analysis of samples obtained by systematic rejection of sparser structure elements allows us to reveal the characteristics of typical structures. These data can be compared with similar results obtained for the LCRS (cf. LCRS1). The analysis was performed for the SCDM and OCDM models at $z = 0$, and for the ΛCDM model at $z = 0$ and $z = 1$.

For the core-sampling analysis a set of 196 cylinders with a radius of $1.7\,h^{-1}$ Mpc was prepared both in comoving and in redshift space. The mean number of points within the cylindrical cores amounts to ~400–600. The analysis was performed for 16 values of the cylinder radius, $1.7\,h^{-1}$ Mpc $\ge r_{cyl} \ge 0.7\,h^{-1}$ Mpc. The separation of sheet-like elements, D_s, and the surface density of the filamentary component, $\sigma_f = D_f^{-2}$, are plotted in Fig. 4 versus the fraction of matter f remaining after rejection of sparse structure elements. It shows the OCDM and ΛCDM models in redshift space at $z = 0$. The parameters typical for the reliable structure elements are marked in Fig. 4 by dotted lines and listed in Table 3 together with similar parameters obtained for the LCRS (LCRS1). Results are found to be close both in comoving and redshift space, and they coincide with the parameter range estimated for the LCRS.

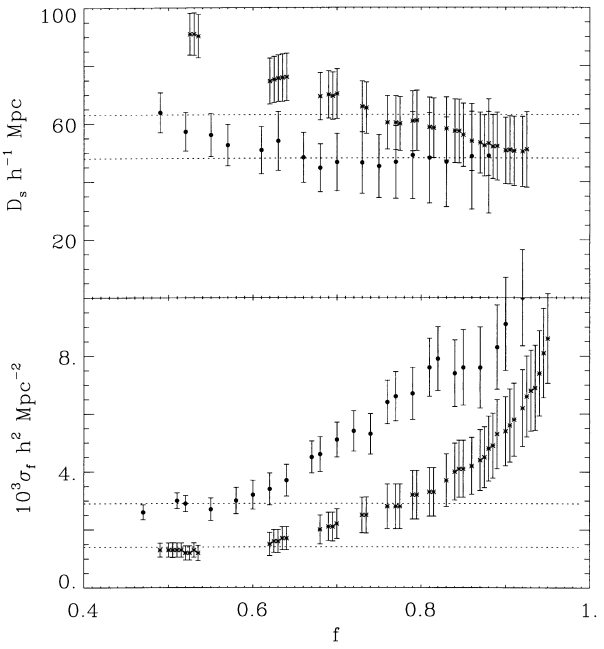

Figure 4. Mean separation of the RSE, D_s, and the surface density of filamentary component, σ_f, versus the matter fraction concentrated within the structures, f, in redshift space, and at $z = 0$, for the OCDM (dots) and ΛCDM (stars) models.

Table 3. Structure parameters with the core-sampling method in redshift space. The threshold N_{thr} is the minimal richness of the considered structure elements, D_s, D_f, and D_f^{min} are the mean separation of sheet-like elements and rich and poor filaments.

model	z	N_{thr}	D_s h^{-1} Mpc	D_f h^{-1} Mpc	D_f^{min} h^{-1} Mpc
LCRS	0.	–	55. ± 7	26.7 ± 3.	10.5 ± 1.
SCDM	0.	8	38. ± 9	19.2 ± 3.	7.5 ± 2.
OCDM	0.	6	48. ± 11	19.2 ± 3.	10.0 ± 3.
ΛCDM	0.	4	63. ± 15	26.7 ± 5.	12.0 ± 4.
ΛCDM	1.	4	45. ± 11	23.6 ± 3.	7.8 ± 2.

In all cases there is a clear signal from the SLSS component, but in contrast with results found for the LCRS, D_s increases slowly for small $f \le (0.6$–$0.7)$. This effect is probably caused by the variation of the covering factor of the sheet-like component, as discussed by Ramella et al. (1992) and Buryak et al. (1994). This effect is less prominent for the OCDM model for which the disruption of RSE measured by the velocity dispersions, σ_1, σ_2 and σ_3, is also less significant. The weak variation of $D_s(f)$ and the quick drop of σ_f with f shows that a significant matter fraction (~0.4–0.5) is associated with the high dense sheet-like component, which is also consistent with the observational results in the LCRS (LCRS1). A population of rich filaments can be identified in Fig. 4, but in contrast with results from the LCRS, it is less representative. For the SCDM model we also found a strong variation of the number of particles from core to core. This is probably caused by the strong disruption of structure elements.

Table 4. Proper sizes of rich structure elements. All mean sizes and dispersions are given by (6.2), (6.4) and Section 6.5 and are measured in h^{-1} Mpc.

model	z	$r_{\rm link}$	$\langle N_{\rm mem}\rangle$	$\langle\lambda\rangle$	σ_λ	$\langle\omega\rangle$	σ_ω	$\langle\theta\rangle$	σ_θ	$\langle D_{\rm prw}\rangle$	$\sigma_{\rm prw}$	$\langle D_{\rm sep}\rangle$	$\sigma_{\rm sep}$
LCRS	0			25.3	6.0	12.3	3.1	5.7	1.3	26.4	1.4	∼38.	∼28.
SCDM-cm	0	0.75	731	9.2	4.0	4.3	1.4	2.7	0.6	16.4	0.6	–	–
SCDM-rs	0	0.75	870	22.8	6.6	7.0	2.6	3.6	0.9	16.0	1.6	–	–
OCDM-cm	0	0.95	907	24.2	7.8	12.1	4.4	6.0	1.9	17.3	1.7	40.3	30.3
OCDM-rs	0	0.95	998	24.4	6.8	12.5	3.2	7.2	1.7	18.3	1.6	37.6	28.3
ΛCDM-cm	0	1.0	801	14.2	6.2	6.2	2.1	3.6	0.9	22.2	1.3	68.4	63.1
ΛCDM-rs	0	1.0	919	21.8	5.5	9.9	2.9	5.0	1.4	23.2	1.2	64.9	57.1
ΛCDM-cm	1	1.0	588	19.6	6.1	7.8	1.8	4.6	1.3	21.4	1.2	79.5	64.0
ΛCDM-rs	1	1.0	641	19.7	4.4	9.1	2.1	4.8	1.1	21.1	0.9	76.3	62.2

The parameters $D_{\rm f}^{\rm min}$ listed in Table 3 corresponds to the minimal separations of filaments found in our analysis at $f \to 1$. As it is common in simulations, the identification of poor filaments is difficult, and their parameters depend on the rejected background. It is well known that for a CDM power spectrum, very small DM pancakes form early, and the estimates of the minimum pancake size in simulations reflect the resolution (in our case given by the size of the computation cells). This means that $D_{\rm f}^{\rm min}$ listed in Table 3 generally characterizes the procedure of background rejection rather than properties of poor structure elements. This problem was discussed in detail by Doroshkevich et al. (1997a, 1998b). The uncertainties in our estimates of $D_{\rm s}$ and $D_{\rm f}$ are larger than those obtained for the LCRS. This shows that simulated DM structures are not fully consistent with the geometrical model on which the core-sampling method is based.

The comparison of structure parameters found for the ΛCDM models at $z = 0$ and $z = 1$ shows the moderate evolution of structure which is approximately consistent with theoretical expectations (Demiański & Doroshkevich 1999b).

6 PROPERTIES OF RICH STRUCTURE ELEMENTS

The analysis performed in Sections 4 and 5 shows that, in fact, for a significant matter fraction $f_{\rm rse} \sim 0.4$, a strong non-linear matter compression results in the formation of massive high-density RSE. The existence of such RSE is a very essential feature of the large-scale matter distribution. A more detailed analysis and the statistical description of RSE is described in this section.

6.1 Discrimination of rich structure elements

The subsamples of RSE were identified and analysed at redshift $z = 0$ in comoving and redshift space for the ΛCDM, OCDM and SCDM models, and for estimating the evolution, a similar subsample of RSE was also analysed at redshift $z = 1$ for the ΛCDM model. As described in Section 4, the RSE were identified with rich clusters found for a suitable linking length, $r_{\rm link}$, and a richness threshold, $N_{\rm mem} \geq N_{\rm thr}$. The probability distribution functions discussed below depend on the definition of a structure element used, and in our approach, on these two parameters. The employed parameters of the subsamples are listed in Table 4.

In the SCDM model, RSE are defined with linking lengths $b^3 \sim 0.48$, that corresponds to a threshold density of clusters $n_{\rm thr} \geq 2.1\langle n_{\rm p}\rangle$, whereas for OCDM and ΛCDM models $b^3 \sim 0.9$ provides better results. For these samples, a significant fraction $f_{\rm rse} \sim 0.4$ of all matter is contained in massive overdensity clumps with $N_{\rm mem} \geq N_{\rm thr} = 200$. The chosen values of b^3 are about 2–4 times smaller than the percolation threshold, $b^3_{\rm perc}$, also listed in Table 2. This means that the RSE defined by these thresholds are actually isolated. Some parameters discussed below, in particular the comoving sizes, depend on the chosen b^3, and they increase for larger b^3 and/or larger $N_{\rm thr}$.

These parameters are the basis for our selection of RSE in simulations. A more detailed comparison of observed and simulated RSE implies an identification of 'galaxies' in the simulated DM distribution (see Section 8).

In the LCRS a similar fraction of galaxies, $f_{\rm gal} \sim 0.4$, is concentrated in clusters defined with a threshold linking length of $b^{-3} \sim 1$–0.5, and a mean overdensity in the RSE of ∼10 (LCRS2). This difference between the threshold densities of RSE used in simulations and in the LCRS is caused in the main by the construction of the LCRS as a set of six slices with angular size $1\overset{\circ}{.}5$ and the effective thickness $\sim(6$–$7)\,h^{-1}$ Mpc only.

The impact of the slice thickness was tested using the mock catalogues prepared by Cole et al. (1998). It was found that the random intersections of RSE with relatively thin slices result in an artificial destruction of selected RSE. It is seen as the growth of the threshold linking length required for the selection of RSE and as stronger random variations of RSE properties with the linking length. Thus, it was found that for the full mock catalogues about (40–45) per cent of 'galaxies' are incorporated in RSE already at $b^3 \sim 1$ which is close to the values used above. In contrast, for the slices with angular size $1\overset{\circ}{.}5$ the same 'galaxy' concentration in RSE is reached for $b^3 \sim 1.5$–2 which is comparable with that used for the LCRS (LCRS2). The small slice thickness also depresses the percolation and restricts the sizes of the richest RSE in the LCRS. The random mixture of fields observed with 50 and 112 fibres (in four slices of the LCRS) amplifies this artificial destruction of selected RSE.

6.2 Mass functions of rich structure elements

The mass function of rich structure elements is written as

$$W_{\rm m} = \frac{N_{\rm mem}}{N_{\rm p}} N_{\rm rse}(\nu),\ \ \nu = N_{\rm mem}/\langle N_{\rm mem}\rangle, \tag{6.1}$$

where $N_{\rm mem}$ and $N_{\rm p}$ are the numbers of points in the cluster and in the sample as a whole, $N_{\rm rse}$ is the number of RSE elements for a given richness ν, and $\langle N_{\rm mem}\rangle$ is the mean number of points per RSE element. This function depends on the degree of matter concentration in RSE, and on the disruption of structures. This disruption divides the large structure elements into a system of high-density clumps bridged by low-density regions, and it also increases the

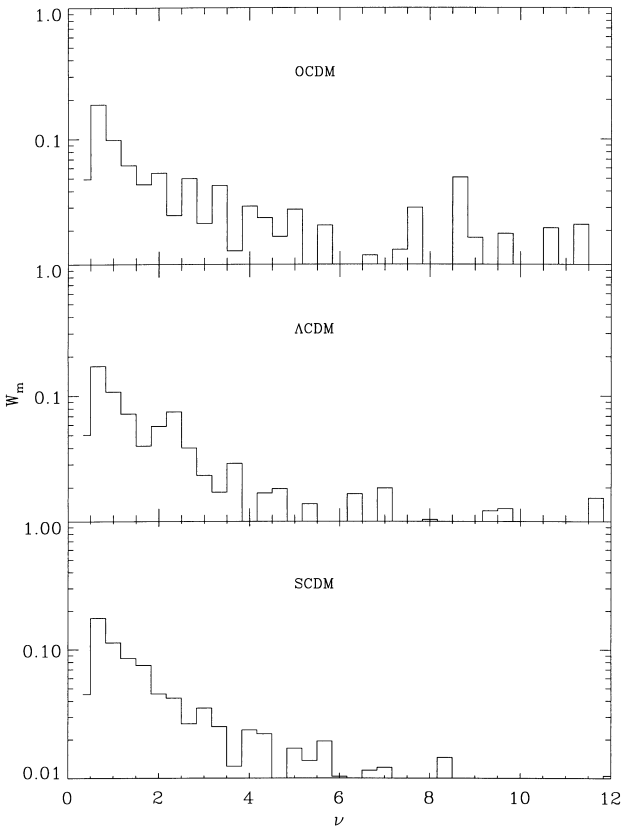

Figure 5. Mass function, $W_{\rm m}$, for the OCDM, ΛCDM and SCDM models in redshift space. Samples and model parameters are listed in Tables 1, 2 and 4.

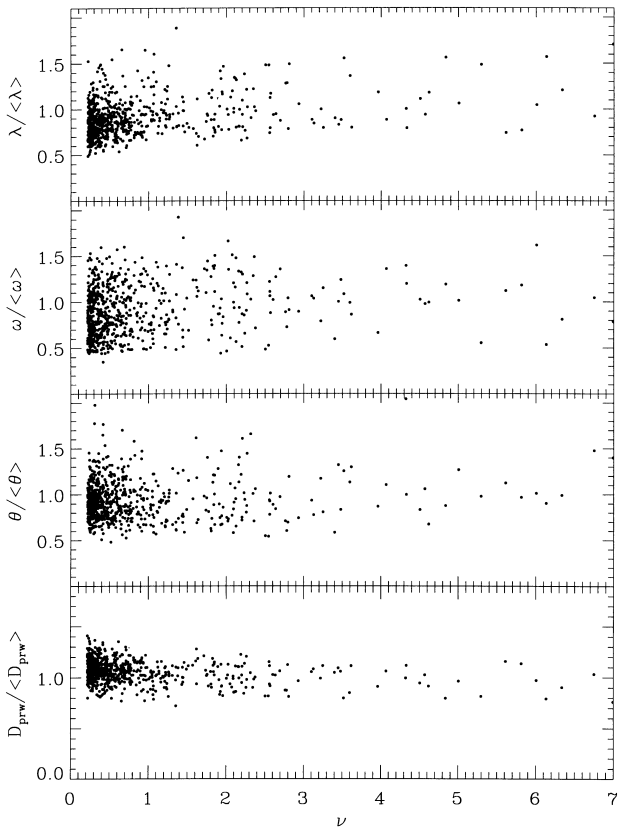

Figure 6. The proper sizes of the RSE, $\lambda/\langle\lambda\rangle$, $\omega/\langle\omega\rangle$ and $\theta/\langle\theta\rangle$, and the size of 'proto-walls', $D_{\rm prw}/\langle D_{\rm prw}\rangle$, versus the mass (richness) of the element, $\nu = N_{\rm mem}/\langle N_{\rm mem}\rangle$, for the ΛCDM model in redshift space at $z = 0$.

fraction of low-mass elements. The rate of disruption depends on the density contrast and, therefore, it is sensitive to the cosmological parameters.

The mass functions are plotted in Fig. 5 for the OCDM, ΛCDM and SCDM models as determined in redshift space. The general character of the functions is very similar in these three models. Some excess of RSE in the tail, i.e. for masses $\nu > 3$–4, are found in the OCDM and ΛCDM models. The threshold richness cuts off the distribution at small masses, and it influences the value of the mean richness of the RSE, $\langle N_{\rm mem}\rangle$. The mean values are listed in Table 4 for all models under investigation.

These mass functions are in general similar to the observed one in the LCRS (LCRS2), and at $\nu \leq 6$ they can also be fitted by a simple exponential law. In both cases, there are a few huge clusters with mass $\nu \sim 5$–10 which accumulate ∼10 per cent of points in the simulations. The rejection of low-mass structure elements has a strong influence on the extent of the mass function.

6.3 The proper sizes of the rich structure elements

The proper sizes of rich structure elements are found with the inertia tensor method, applied to the subsample of RSE. All proper sizes depend on the mass of the RSE. The scaling can be approximated by

$$L = \nu^{1/3}\lambda, \quad w = \nu^{1/3}\omega, \quad t = \nu^{1/3}\theta, \tag{6.2}$$

$$\sim 0.2 \leq \nu = N_{\rm mem}/\langle N_{\rm mem}\rangle \leq 7.$$

The mass-averaged length $\langle\lambda\rangle$, width $\langle\omega\rangle$ and thickness $\langle\theta\rangle$ of clusters are listed in Table 4 together with the corresponding dispersions. Scatter plots of these values versus the richness of RSE ν for the ΛCDM model are shown in Fig. 6. The distributions of proper sizes λ, ω, and θ, are similar to Gaussian distributions with mean values and dispersions listed in Table 4.

The scaling (6.2) describes well the mass dependence of the proper sizes that results from the relatively regular shape of RSE and the moderate influence of boundary effects. In the LCRS a similar scaling is found for the two larger sizes, whereas the small size is weakly dependent on the richness (LCRS2). This is probably caused by the special construction of the LCRS as a set of thin slices. The strong richness dependence found for the Durham/UKST redshift survey (Doroshkevich et al. 1999) could be caused by the relatively small size of the survey.

Results listed in Table 4 show that for the OCDM and ΛCDM models, all proper sizes are found to be close (in the range of the dispersion) to the sizes observed in the LCRS. Moderate variations of the threshold linking lengths do not change the mean characteristics of the RSE, but the sizes of the largest structure elements are sensitive to such variations.

For the SCDM model, all mean proper sizes in redshift space exceed the sizes found in comoving space. These differences become smaller for the ΛCDM and the OCDM models, and they decrease with increasing redshift as is shown by the comparison of the ΛCDM model at $z = 0$ and $z = 1$. It is explained, in part, by the well known influence of the velocity dispersion ('finger of God effect'). This effect also depresses the small-scale clustering, however, and, apparently, partly cancels the disruption of large structure elements typical for the non-linear evolution of pancakes. This is clearly seen in the growth of the mean length $\langle\lambda\rangle$, which

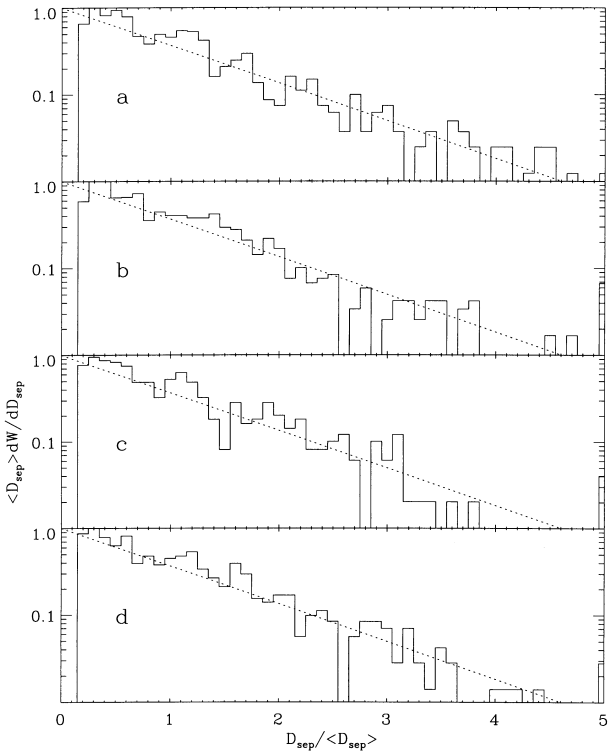

Figure 7. The frequency distribution $\langle D_{\rm sep}\rangle {\rm d}W/{\rm d}D_{\rm sep}$ of separation of the RSE in comoving (panels a and c) and redshift (panels b and d) space at $z = 0$ (panels a and b) and $z = 1$ (panels c and d). The exponential fits are shown by dotted lines.

exceeds any velocity dispersions and, therefore, is insensitive to the 'finger of God' effect. In contrast, the influence of the small-scale clustering on the thickness of structure elements is not so strong, and its growth in redshift space is probably caused by the direct influence of small-scale velocities. Hence, we can take the value $\langle L\rangle$ in redshift space as a genuine diameter of the RSE, and the value $\langle t\rangle$ from comoving space as real thickness. For the middle size, $\langle w\rangle$, both effects can be important.

6.4 The 'proto-size' of the rich structure elements

The measured parameters of RSE allow us also to estimate the volume which initially contained all matter in RSE, and the degree of compression connected with its formation. A simple model was used for this estimate in LCRS2. As the lengths of the RSE exceed the two other sizes, we can neglect the matter compression along this axis, and we can consider the RSE formation as a 2D matter infall to the gravitational well. In this case we can obtain a simple estimate using mass conservation:

$$\langle n_{\rm rse} tw\rangle \approx \langle n_{\rm p}\rangle\langle t_0 w_0\rangle \approx \langle n_{\rm p}\rangle L^2_{\rm prw}, \tag{6.3}$$

$$L^2_{\rm prw} = \frac{6N_{\rm mem}}{\pi L\langle n_{\rm p}\rangle}, \quad L_{\rm prw} \le L\,,$$

where $n_{\rm rse}$ and $\langle n_{\rm p}\rangle$ are the comoving number density of particles within the RSE and in the sample as a whole, respectively, t and w are the thickness and width of the RSE, and t_0, w_0 and $L_{\rm prw} = \sqrt{w_0 t_0}$ are the typical sizes of the 'proto-structures', defined in the initially almost homogeneous matter distribution. The mass dependence can be described similarly to equation (6.2):

$$L_{\rm prw} = \nu^{1/3} D_{\rm prw}. \tag{6.4}$$

The distributions of $D_{\rm prw}$ are also similar to Gaussian distributions with the mean values, $\langle D_{\rm prw}\rangle$, and dispersions, $\sigma_{\rm prw}$, listed in Table 4. The comparison of ω and θ with $D_{\rm prw}$ shows that at $z = 0$ the RSE formation can be roughly described as an asymmetric matter compression by a factor of $\sim$2 along the middle axis (w), and a factor of $\sim$4–5 along the shorter axis (t). At $z = 1$ the corresponding compression factors are $\sim$1.5 times smaller. For the high-density clumps at redshift $z = 3$ in the ΛCDM model the size of the 'proto-structures' is

$$L_{\rm prw}(z = 3) \approx (18 \pm 3.5) h^{-1}{\rm Mpc}. \tag{6.5}$$

The values $D_{\rm prw}$ are plotted in Fig. 6 for given samples of RSE of the ΛCDM model. The parameters are very stable, in particular, they depend only weakly on the sample under investigation, and on the linking length, since usually the growth of the cluster sizes is accompanied by a drop in the number density. They are sensitive to the possible bias between the spatial distribution of DM and galaxies, however.

6.5 The mean separation of the structure elements

The mean separation of RSE can be found, applying a simple version of the core-sampling method for subsamples of RSE. A sample of 250 rectangular cores with sides $10\,h^{-1}$ Mpc$\times$ $10\,h^{-1}$ Mpc, oriented along one axis (the axis where the redshift distortions are added) and containing all particles of RSE, was prepared for the ΛCDM and OCDM models both in comoving and in redshift space for $z = 0$ and for the ΛCDM model at $z = 1$. All particles are projected on the axis of the cores, and they are collected in clusters with the linking length, $r_{\rm link}$, used for the RSE preparation (Table 4). The mean separation between these clusters (the 'mean free-path' between the RSE), $\langle D_{\rm sep}\rangle$, and the dispersions, $\sigma_{\rm sep}$, are listed in Table 4. The large dispersion – more than 50 per cent of the mean value – is typical for an exponential Poisson-like distribution. The frequency distribution of cluster separations is plotted in Fig.7 together with the best exponential fit. The mean separation of the RSE depends weakly on the redshift, and it is consistent with the mean separation of wall-like elements found with the core-sampling approach in Section 5. For the OCDM model the numerical estimates are consistent with that found in the LCRS (cf. LCRS2), but for the ΛCDM model they exceed the observed values by a factor of $\sim$1.5.

The mean separation of RSE (or the 1D number density) allows us to obtain an independent estimate of the relative richness of RSE for a given subsample, i.e. for some linking length b and threshold $N_{\rm thr}$, or a certain matter fraction in RSE, $f_{\rm rse}$. The difference found above for the ΛCDM model indicates that in this case the same fraction of particles is concentrated in a smaller number of RSE. To eliminate this difference, a threshold richness $N_{\rm thr} \sim 150$ could be used, which has small effects on the other parameters of RSE.

The mean separations between structure elements of the filamentary component and their dispersions, $\langle D_{\rm f}\rangle$ and σ_D, can be found through a similar analysis of subsamples prepared by removing all RSE from the full sample. We obtain $\langle D_{\rm f}\rangle \sim 9\,h^{-1}$ Mpc, $\sigma_D \sim 6.5\,h^{-1}$ Mpc, for the OCDM model, and $\langle D_{\rm f}\rangle \sim 14\,h^{-1}$ Mpc, $\sigma_D \sim 10.5\,h^{-1}$ Mpc, for the ΛCDM model. This data agree well with the value $D^{\rm min}_{\rm f}$ listed in Table 3 for the LCRS.

6.6 Inner structure of RSE and LDR

The point distribution in a sample can be characterized with the

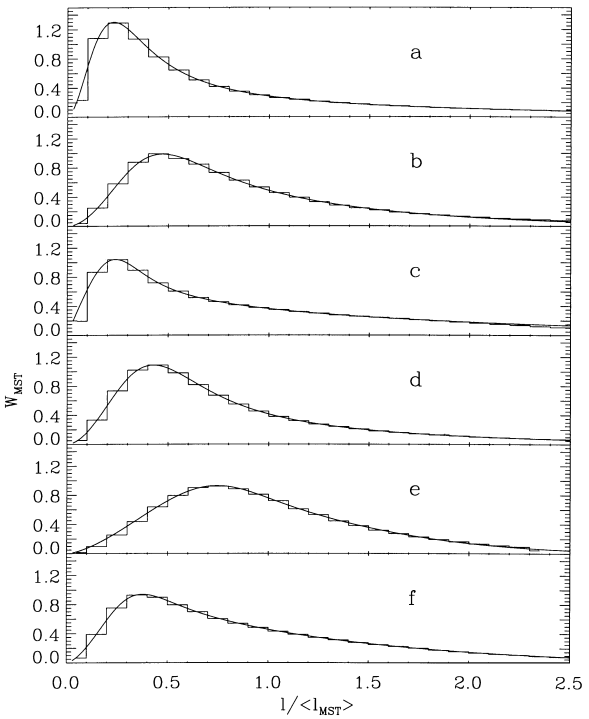

Figure 8. The frequency distribution of the edges of MST for the ΛCDM model. Samples are marked and sample parameters are listed in Table 5. The fit of FDMST to relation (3.1) is shown by the solid line.

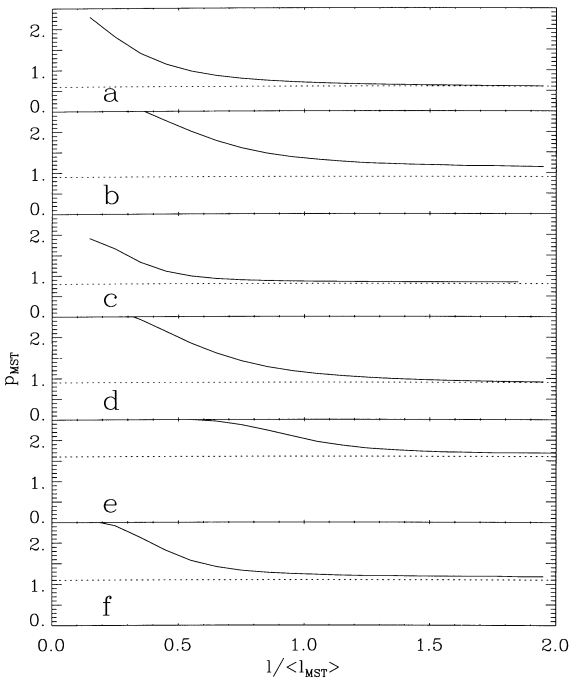

Figure 9. Variations of power indices p_{MST} for the same samples of the ΛCDM model as in Fig. 8. Sample parameters are listed in Table 5. The fit of FDMST to relation (3.1) is shown by the solid line.

NCLL and the MST techniques as described in Section 3. These methods allow us to discriminate between the dominance of filamentary and sheet-like structures in a point sample, and to characterize the point distribution within separate structure elements. In this sense, the methods are complementary to the core-sampling approach. Thus, for the filamentary component, power indices p_t and $p_{MST} \sim 1$ can be expected, whereas for the sheet-like component, the appearance of power indices p_t and $p_{MST} \sim 2$ seems to be more typical.

Here we apply these methods to the ΛCDM model. We analyse separately the full sample, the RSE, and the LDR, the latter are obtained by removal of RSE from the full sample. The main results are presented in Figs 8 and 9, and they are collected in Table 5, where $\langle l_{MST}\rangle$ is the mean edge length of the MST and

$$b_{MST} = \left(\frac{4\pi}{3}\langle n_p\rangle\right)^{1/3}\langle l_{MST}\rangle. \qquad (6.6)$$

Here $\langle n_p\rangle$ is the mean number density in the sample under consideration.

The FDMST are plotted in Fig. 8 for the full sample and for the RSE and LDR, both in comoving and in redshift spaces, and at $z = 0$. The variation of the power indices versus the edge lengths is plotted in Fig. 9. The left-hand side of the FDMST describes the matter condensation within high-density clumps that form the inner structure of filaments and walls. It is similar for all subsamples. The right-hand side of the FDMST characterizes the relative positions of these clumps and other particles of the subsamples.

These figures demonstrate that in the comoving space for all samples, $p_{MST} \sim 1$ for edge lengths $l/\langle l_{MST}\rangle \geq 0.5$–1. The NCLL method confirms that $p_t \sim 1$ is reached for $b \geq 0.5$, this is about 1.6 times smaller than $b \sim 0.8$ used for the RSE discrimination, and ~2.5 times smaller than the value b_{perc} listed in Table 2. These values emphasize the joint character of the point distribution both within RSE and LDR which can be interpreted as a predominantly 1D Poisson distribution typical for filaments. The mean edge length of the MST, $\langle l_{MST}\rangle$, in the RSE is ~2–3 times smaller than within LDR but variations of b_{MST} do not exceed ~20 per cent. In redshift space the impact of the velocity dispersion erases the small-scale structure of RSE. Therefore we find an apparent particle distribution similar to a 2D Poisson distribution.

The characteristics obtained both with the NCLL and MST methods are similar to each other within the range of statistical

Table 5. Fit parameters for the FDMST and for the cluster distribution, p_t, for full samples, RSE and LDR for the ΛCDM model.

sample	$\langle l_{MST}\rangle$	b_{MST}	p_{MST} h^{-1} Mpc	p_t
		$z = 0$, comoving space		
a TOT	0.72	0.72	0.60 ± 0.02	0.59 ± 0.03
b RSE	0.30	0.62	1.11 ± 0.02	1.02 ± 0.05
c LDR	1.00	0.80	0.83 ± 0.02	0.99 ± 0.03
		$z = 0$, redshift space		
d TOT	0.78	0.78	0.91 ± 0.03	0.85 ± 0.04
e RSE	0.42	0.83	1.60 ± 0.04	1.83 ± 0.03
f LDR	1.00	0.80	1.11 ± 0.03	1.11 ± 0.02
		$z = 1$, comoving space		
TOT	0.90	0.90	0.76 ± 0.03	0.97 ± 0.03
RSE	0.35	0.69	1.0 ± 0.03	1.30 ± 0.05
LDR	1.00	0.80	0.87 ± 0.03	1.10 ± 0.02
		$z = 1$, redshift space		
TOT	0.91	0.91	0.97 ± 0.02	1.02 ± 0.02
RSE	0.45	0.89	1.4 ± 0.05	1.93 ± 0.02
LDR	1.00	0.80	1.1 ± 0.03	1.20 ± 0.03

uncertainty. In any case, independent of the geometrical interpretation, the power indices and typical scales that characterize the spatial matter distribution in the RSE and LDR are essentially different, and this verifies the accepted discrimination of these regions. These results agree well with estimates of the mean overdensity, $\delta_{\rm rse}$, listed in Table 2 and obtained in other way. They confirm the essential concentration of high density clumps in RSE.

The results obtained for the LDR are consistent with the dominance of a filamentary component. For the RSE, the unexpected value of the power index in the comoving space can be considered as an indirect evidence in favor of RSE formation from earlier formed filaments. It can also be traced back to different factors, such as the wall disruption and the limited resolution of simulations and, therefore, further investigations are required.

In the LCRS a power index $p_{\rm t} \sim p_{\rm MST} \sim 1.7$ has been found for RSE, and $p_{\rm t} \sim p_{\rm MST} \sim 1$ for LDR and for the total sample (LCRS2). This is comparable with our results for the redshift space listed in Table 5. The complicated inner structure of RSE is also seen in the LCRS and, more clearly, in the galaxy distribution within the Great Wall (fig. 5 in Ramella, Geller, & Huchra 1992).

7 CHARACTERISTICS OF THE EXPECTED AND SIMULATED DM STRUCTURE

The reproduction of the main observed characteristics of the RSE in simulations with a standard CDM-like power spectrum verifies that the observed structure was formed during the non-linear evolution of small initial perturbations, and, therefore, the characteristics of structure can be expressed through the parameters of a suitable initial power spectrum of Gaussian fluctuations for a specific cosmological model. Statistical characteristics of the DM structure based on Zel'dovich's non-linear theory of gravitational instability (Zel'dovich 1970,1978; Shandarin & Zel'dovich 1989) were discussed by Demiański & Doroshkevich (1999a,b). The approximate expressions derived therein connect some of these characteristics to the parameters of the cosmological model. The comparison of the approximate analytic results and the simulations reveals both the influence of factors omitted in the theoretical description and random factors distorting the simulated structure.

The surface density of RSE and velocity dispersions within RSE, and the velocity of structure elements seem to be most interesting. These values can be found using the simple version of core-sampling described in Section 6.5. We characterize the mass of each cluster within the rectangular sampling cores by the surface density of structure elements, m_w, and the velocity dispersion within clusters also along the core, σ_r. These values can be found for the RSE. We consider also the dispersion of 1D velocity of clusters along the core, σ_q, which can be found for the full samples, and for the RSE and the filamentary subsamples of structure elements separately. Some of these characteristics can be compared with similar 3D characteristics discussed above for RSE that demonstrate the influence of the sample selection and the averaging procedure.

The theoretical parameters are expressed through the typical length-scale, l_0, linked to the initial power spectrum, and typical dimensionless 'time', τ_0, linked to the velocity dispersion, $\sigma_{\rm vel}$, and the parameter σ_8 listed in Table 1 as

$$l_0^{-2} = \int_{k_{\rm min}}^{k_{\rm max}} kT(k){\rm d}k, \quad l_0 \approx \frac{6.6}{\Omega_{\rm m} h} h^{-1}{\rm Mpc},$$

$$\tau_0 = \frac{\sigma_{\rm vel}}{\sqrt{3}\beta l_0 H_0}, \quad \beta \approx (0.43 + 0.57\Omega_{\rm m})^{-1}, \tag{7.1}$$

$$\tau_0 = 0.55\sigma_8(\Omega_{\rm m}h)^{0.438}\left[1 + 5.657(\Omega_{\rm m}h)^{1.4}\right]^{0.562},$$

where k is the comoving wave number, $k_{\rm min} = 2\pi/L_{\rm box}$, $k_{\rm max} = k_{\rm min}N_{\rm cell}^{1/3}$, and $T(k)$ is a transfer function. The 'time' τ_0 characterizes the amplitude of perturbations and the reached period of structure evolution. For the SCDM, OCDM and ΛCDM simulations we have

$$\begin{aligned} &l_0 = 13.2,\ 22,\ \text{and}\ 26.9\,h^{-1}{\rm Mpc},\\ &\tau_0 = \tau_{\rm vel} = 0.43,\ 0.27\ \text{and}\ 0.37\\ &\tau_0 = \tau_8 = 0.81,\ 0.31\ \text{and}\ 0.46. \end{aligned} \tag{7.2}$$

and differences between values $\tau_{\rm vel}$ & τ_8 characterize the sensitivity of various estimates of amplitude to the small scale matter clustering. The velocity dispersions σ_r and σ_q are given in $\rm km\,s^{-1}$. For Gaussian initial perturbations the distribution of pancake velocities along a core is expected also to be Gaussian with a negligible mean velocity and a dispersion

$$\sigma_q \approx \sigma_{\rm vel}/3 = H_0 l_0 \beta\tau_0/\sqrt{3}. \tag{7.3}$$

Here a random orientation of pancakes with respect to the sampling cores is taken into account.

In this case the distribution of surface density of RSE, m_w, can be expressed as follows:

$$N_w = \frac{a_w}{\sqrt{x}}{\rm e}^{-x} erf(\sqrt{x}), \quad x = \frac{b_w m_w}{\langle m_w\rangle}, \tag{7.4}$$

$$\mu_w = \frac{\langle m_w\rangle}{b_w\langle n_{\rm p}\rangle l_0} \approx 8(0.5 + 1/\pi)\tau_0^2 = 6.6\tau_0^2,$$

where a_w and b_w are fit parameters. The expected distribution of the filamentary component is described by a more cumbersome relation.

An expression like (7.4) with parameters a_r and b_r and $x = b_r\sigma_r/\langle\sigma_r\rangle$ also describes the distribution of the 1D inner velocity dispersion along the core, σ_r. For RSE this dispersion can be expressed through l_0 and τ_0 as

$$\mu_r = \frac{\sqrt{\langle\sigma_r^2\rangle}}{b_r H_0 l_0 \beta} \approx \frac{1}{2\sqrt{3}}\frac{\langle m_r\rangle}{\langle n_{\rm p}\rangle l_0} \approx \frac{3.3\tau_0^2}{\sqrt{3}} \approx \tau_0\frac{3.3\sigma_q}{H_0 l_0 \beta}. \tag{7.5}$$

Using this relation we can measure the mean surface mass density of RSE $\langle m_r\rangle$ by the velocity dispersion.

These relations allow us to estimate the model parameters l_0 and τ_0 using the measured surface density of RSE $\langle m_w\rangle$, the velocity dispersion within RSE, σ_r, and the velocity dispersions of various populations of structure elements, σ_q. To suppress the impact of small-scale clustering, the analysis was performed for the subsample of RSE with the core side $10\,h^{-1}$ Mpc. Because of the small separation of filaments, for the full sample and subsample of LDR, discussed in Section 6.6, a core side $4\,h^{-1}$ Mpc was used.

For RSE the measured distributions of surface density , m_w, and velocity dispersion, σ_r, are plotted in Figs 10 and 11 together with the best fits (7.4). The measured parameters are listed in Table 6, the theoretical expectations are given by equation (7.2). The distribution of pancake velocities is well fitted to the Gaussian function with dispersion σ_q listed in Table 6.

These velocity dispersions are smaller by about 20 per cent than those listed in Table 2, which demonstrates the influence of averaging procedures in obtaining the final parameters.

The values τ_0, averaged over the measurements listed in Table 6, are

$$\langle\tau_0\rangle \approx 0.58 \pm 0.09,\ \approx 0.29 \pm 0.03,\ \approx 0.40 \pm 0.05, \tag{7.6}$$

Table 6. Characteristics of mass and velocity distributions in comoving space for the full samples, RSE and LDR for the SCDM, OCDM and ΛCDM model. $\mu_r = \langle m_r\rangle/(\langle n_p\rangle l_0) \approx 8\tau_r^2$, $\mu_w = \langle m_w\rangle/(\langle n_p\rangle l_0) \approx 8\tau_w^2$, the velocity dispersions σ_r and σ_q are given in km s^{-1}.

sample	σ_q	σ_r	μ_w	τ_w	μ_r	τ_r	τ_q
			SCDM				
TOT	501	230	–	–			0.66
RSE	442	492	1.4	0.50	1.29	0.44	0.65
LDR	508	151	–	–	–	–	0.66
			OCDM				
TOT	263	98	–	–	–	–	0.30
RSE	245	250	0.8	0.35	0.41	0.25	0.28
LDR	277	76	–	–	–	–	0.32
			ΛCDM				
TOT	360	155	–	–	–	–	0.42
RSE	351	412	1.3	0.44	0.63	0.31	0.40
LDR	374	119	–	–	–	–	0.44

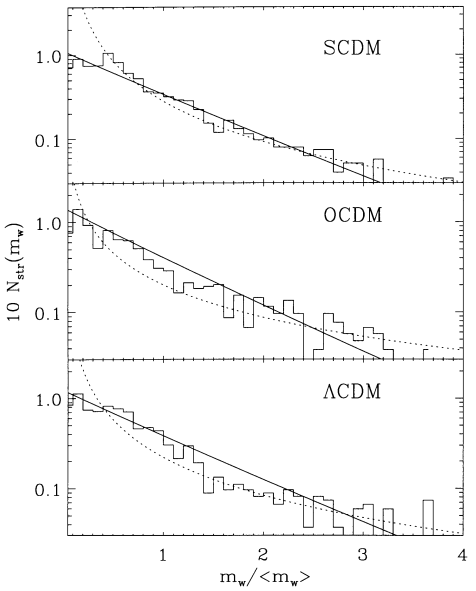

Figure 10. The distribution of the mass surface density of RSE. The best fit (7.3) is shown by solid lines, the best-fitting power law is plotted by dotted lines.

for the SCDM, OCDM and ΛCDM models. Differences between these values and estimates of τ_0 given in (7.2) characterize the influence of random factors such as the selection and disruption of structure elements and the real precision reached.

The measured distributions of the surface density of RSE are also well fitted by power laws with exponents $\kappa \sim 1.7$ that may result from the strong wall disruption. The power law can be reproduced analytically, assuming a set of clusters with spherically symmetric surface densities falling off according to a power law $\sigma_{cls} \propto r^{-\gamma}$. In this case the mass function of clusters in cores is also expressed by a power law as

$$N_{cor} dm_w \propto \sigma_{cls} r dr \propto \sigma_{cls}^{-2/\gamma} d\sigma_{cls}, \qquad (7.7)$$

with an exponent $\kappa = 2/\gamma$. For $\kappa \sim 1.7$ we have $\gamma \sim 1.2$, which is close to the well-known King's law, $\sigma_{cls} \propto (1 + r^2/r_c^2)^{-1/2}, \gamma \sim 1$, widely used to fit to the density profiles of elliptical galaxies.

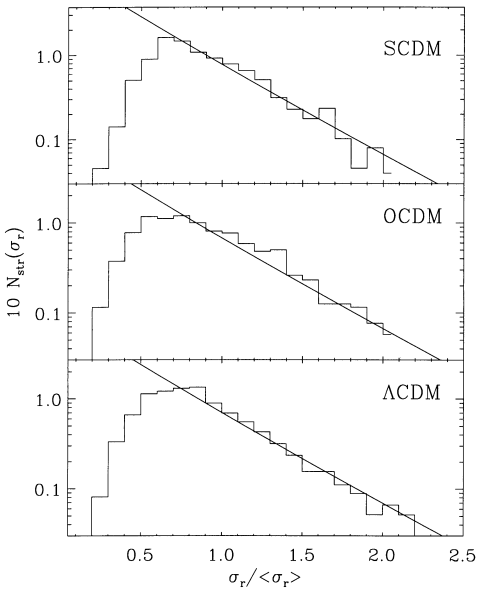

Figure 11. The distribution of velocity dispersions σ_r for the RSE. The best fit (7.3) is shown by solid lines.

8 ANALYSIS OF MOCK CATALOGUES

For a DM-dominated universe the analysis of DM structures is very important in itself as the feedback of baryonic matter and galaxy formation to the DM evolution on scales larger than the mean intergalactic separation is small. On the other hand, almost all observed characteristics of the large-scale structure are obtained for the galaxy distribution alone, and the galaxy distribution may be biased in comparison with the distribution of DM. Further, all observed galaxy catalogues suffer from selection effects that influence our cosmological conclusions.

The selection effects are well studied and reproduced in available mock catalogues (see, e.g., Cole et al. 1998). A preliminary analysis of these catalogues reveals, for example, some distortions of observed parameters of RSE caused by the small angular size of the LCRS (see discussion in Section 6). More detailed analysis of these catalogues with the technique described above is in preparation. It allows us to find the optimal strategy of data analysis that suppresses the influence of selection effects.

A much more complicated problem is the possible bias between the DM and the galaxy distribution. The properties of large-scale structures are moderately sensitive to the small-scale bias (BBKS; Coles 1993; for review, Sahni & Coles 1995), but available observations show that the spatial distribution of DM and luminous matter can be biased on large scales as well. Indeed, while on one hand in clusters of galaxies the observed ratio of galaxy and baryonic densities is found to be $\rho_{gal}/\rho_{gas} \sim 0.2$ (see, e.g., White, Briel & Henry 1993), on the other hand, for example within the Bootes Void, $\rho_{gal}/\rho_{gas} \to 0$ (Weistrop et al. 1992). The existence of 'invisible' structure elements, which are now seen as gas clouds responsible for weak Lyα absorption lines situated far from galaxies (~ 5–$6\,h^{-1}$ Mpc – Morris et al. 1993; Stocke et al. 1995; Shull, Stock & Penton 1996) can also be considered as evidence in favour of a large-scale bias.

Such a large-scale bias could be produced by the UV radiation from the first galaxy population during the reheating of the Universe (Dekel & Silk 1986; Dekel & Rees 1987). Quantitative estimates (Demiański & Doroshkevich 1999a, b, c) show that it can increase the galaxy concentration within the RSE by about a factor of 1.5–2. Indirect

evidence in favor of such a bias was found in simulations by Sahni, Sathyaprakash & Shandarin (1994) as a suppression of structure formation in large regions around the maxima of gravitational potential, and by Doroshkevich, Fong & Makarova (1998) as a difference in the characteristics of spatial distribution of the rare high peaks identified as 'galaxies' and of the main fraction of structure elements in simulated DM distributions. This bias can be essential for reliability of discrimination between cosmological models.

Unfortunately, such large-scale bias cannot be simulated yet, since simulations of the galaxy formation in large boxes with the required resolution are impossible. This means that a bias can only be introduced by hand using simple plausible assumptions. Some such models as discussed by Cole et al. (1998) increase the 'galaxy' concentration within RSE. More detailed tests of these models will be discussed separately.

Here we restrict our consideration to the analysis of simple mock catalogues prepared for the OCDM model. With the spatial and mass resolutions of our simulations ($\sim 10^{11}\,M_\odot$), we are compelled to identify 'galaxies' with selected DM particles. Four mock samples with different clustering properties were prepared and investigated. The simplest sample mock_1 was constructed with a threshold prescription depending on the local environmental density within a sphere of $1\,h^{-1}$ Mpc around the particles. No 'galaxies' are identified with particles with local density smaller than the mean density, and 'galaxy' tracers are selected randomly from the particles in overdense regions. The other catalogues use a smooth probability distribution proportional to the local environmental density within the same scale. The constant of proportionality was chosen to vary the degree of clustering of the mock samples, i.e. to get an autocorrelation function of simulated 'galaxies' in broad agreement with data (for the LCRS, cf. e.g. Tucker et al. 1997). The catalogues were normalized to the mean number density of galaxies, $n_{\rm gal} \sim 2\times 10^{-2}\,h^3\,\mathrm{Mpc}^{-3}$, which is equivalent to the observed galaxy density with a limiting magnitude of about $M_R = -18$.

The sample mock_1 with the threshold bias shows weakly enhanced clustering of the mock 'galaxies' with respect to the dark matter: the correlation function in redshift space shows a power law $(r/r_0)^{-\gamma}$ with a correlation length $r_0 = 6.5\,h^{-1}$ Mpc and a slope $\gamma = 1.4$. The correlation length of DM, also in the redshift space, is $r_0 = 5h^{-1}$ Mpc, and the slope is $\gamma = 1.3$.

The impact of the local environment allows to vary the clustering and to obtain mock samples with different properties. Thus, the weakly clustered sample mock_2 is similar to mock_1 (correlation length in redshift space $r_0 = 6\,h^{-1}$ Mpc, slope $\gamma = 1.4$) while mock_3 is intermediate ($r_0 = 7\,h^{-1}$ Mpc, $\gamma = 1.5$) and mock_4 strongly clustered ($r_0 = 8\,h^{-1}$ Mpc, $\gamma = 1.6$). For the sample mock_2, we impose an additional threshold of no 'galaxy' identification for lower than mean density. We discuss such mock catalogues in our rectangular slices, which allow a direct comparison with the DM catalogue studied above. It demonstrates directly the influence of bias models. This is most important as a first step of the analysis of the influence of bias. The selection criteria required for the more detailed comparison with observed catalogues such as the LCRS (cf. the mock sample for ΛCDM presented in Fig. 1) will be imposed as a next step in a separate paper. The simple models described above reproduce only some features of the large-scale bias and serve mainly as illustration of the potential of the statistics used for the bias discrimination. More realistic models would be sensitive to a broader density environment of particles, i.e. they should be able to follow in more detail the expected interaction of large- and small-scale perturbations. Such models will be studied and discussed separately.

Table 7. Parameters of RSE in mock catalogues in redshift space.

model	$r_{\rm link}$ h^{-1} Mpc	b^3	$N_{\rm thr}$	$N_{\rm rse}$	$f_{\rm rse}$	$\delta_{\rm rse}$
mock_1	2.1	0.626	30	830	0.44	7.7
mock_2	2.0	0.586	35	792	0.43	9
mock_3	1.7	0.554	50	863	0.45	11
mock_4	1.9	0.563	70	509	0.45	14

The first step of our analysis repeats the approach utilized in Section 4 to define the sample of RSE with the required richness and overdensity. Such sets of RSE were found in redshift space for all four mock catalogues with the parameters listed in Table 7. For all mock catalogues the threshold density of RSE was ∼30 per cent larger than that for the DM catalogue. For the mock_1 and mock_2 catalogues, the small value of $N_{\rm thr}$ requires that the reproduction of a sufficient 'galaxy' concentration within the RSE is also accompanied by a relatively low overdensity of RSE. Even so, the overdensity is found to be at least twice as large as for the corresponding DM catalogue (see Table 2), and it is comparable with the overdensity found for the LCRS. For mock_3 and mock_4 catalogues, the parameters of RSE are similar to each other, and to that found for the LCRS, and the overdensities reached are about three times larger than for the DM catalogue. For all mock catalogues the velocity dispersions are the same as those found for DM RSE. These results alone show that the models of bias used provide an essential excess of 'galaxy' concentration within the RSE and, therefore, can be considered as a reasonable basis for further more detailed investigations.

The proper sizes of rich structure elements are found with the inertia tensor method, applied to the subsample of RSE. All proper sizes depend on the mass of the RSE. For all mock catalogues the scaling can be approximated by

$$L = \nu^{0.43}\lambda, \quad w = \nu^{0.46}\omega,$$
$$t = \nu^{0.44}\theta,\ L_{\rm prw} = \nu^{0.33}D_{\rm prw}, \qquad (8.1)$$
$$\sim 0.3 \le \nu = N_{\rm mem}/\langle N_{\rm mem}\rangle \le 25.$$

The mass-averaged length $\langle\lambda\rangle$, width $\langle\omega\rangle$, thickness $\langle\theta\rangle$ and the size of 'proto-wall', $D_{\rm prw}$, are listed in Table 8 together with the corresponding dispersions. The stronger scaling found for the mock catalogues compared with the DM catalogue is also caused by the biasing and therefore this approach can also be used to discriminate between bias models. The main parameters of RSE listed in Table 8 are close to those listed in Table 4 for the OCDM model in redshift space. The shape and power indices found for the FDMST are also close to those listed in Table 5. As before, in comoving space the 1D character of the 'galaxy' distribution dominates, i.e. the exponent $p_{\rm MST} \sim 1$, whereas in redshift space the 'galaxy' distribution within RSE is similar to a 2D Poissonian distribution with the exponent $p_{\rm MST} \sim 2$.

These results show that the discussed methods reveal the influence of the bias models used. The impact of bias is also essential for the less massive structure elements, and especially for the matter and 'galaxy' content in 'voids'. These regions will be investigated further with the MST technique in a separate study.

9 SUMMARY AND DISCUSSION

In this paper the properties of simulated spatial matter distributions were studied for five cosmological models with CDM-like power

Table 8. Proper sizes of RSE in mock catalogues. All mean sizes and dispersions are given by (6.2), (6.4) and Section 6.5 and are measured in h^{-1} Mpc.

model	$r_{\rm link}$	$\langle N_{\rm mem}\rangle$	$\langle\lambda\rangle$	σ_λ	$\langle\omega\rangle$	σ_ω	$\langle\theta\rangle$	σ_θ	$\langle D_{\rm prw}\rangle$	$\sigma_{\rm prw}$	$\langle D_{\rm sep}\rangle$	$\sigma_{\rm sep}$
LCRS			25.3	6.0	12.3	3.1	5.7	1.3	26.4	1.4	∼38	∼28
mock_1-rd	2.1	108	20.1	4.9	10.6	2.0	6.0	1.4	23.0	1.2	62	57
mock_2-rd	2.0	119	19.3	4.4	10.5	2.1	5.9	1.4	23.2	0.9	53	57
mock_3-cm	1.9	179	18.5	6.2	8.4	2.7	4.6	1.3	22.8	1.2	51	53
mock_3-rd	1.7	174	18.3	4.5	9.4	2.2	5.1	1.4	22.9	0.9	49	54
mock_4-rd	1.9	218	21.0	5.1	10.7	2.5	5.4	1.8	27.5	0.8	57	64

spectra. The main parameters of the simulations are listed in Table 1. The simulations were performed in large boxes in order to reproduce correctly the mutual interaction of large- and small-scale perturbations, and to obtain a representative sample of wall-like RSE. The broad set of cosmological models considered allows us to reveal the influence of main cosmological parameters on the formation and evolution of the wall-like RSE, and to discriminate between these models. Our results show that the methods utilized in this paper are effective, and they yield a description of the spatial matter distribution on large scales and, in particular, the characteristics of the RSE.

9.1 Main results

The main results of our analysis can be summarized as follows.

(i) Simulations performed with the standard *COBE*-normalized CDM-like power spectrum reproduce well both the wall-like RSE and the filamentary component of structures in LDR. Each component accumulates an essential fraction of matter, and is equally important for the description of the joint network structure in the large-scale matter distribution.

(ii) The phenomenon of strong matter concentration within the wall-like rich structure elements can also be reproduced for suitable cosmological models. An essential fraction of DM, $f_{\rm rse} \sim 0.4$, is compressed non-linearly on the scales ~ 17–$25\,h^{-1}$ Mpc, i.e. less than the mean separation of these RSE by a factor of ∼2–3.

(iii) The RSE are usually disrupted into a system of high-density clumps, which results in the growth of the inner velocity dispersion. The rate and the degree of disruption depend on the parameters of the cosmological models.

(iv) The comparison of observed and simulated parameters of the wall-like RSE allows us to discriminate between different cosmological models and to reveal the class of models that can reproduce the main observed characteristics of the wall-like RSE. These models are the ΛCDM model with $\Omega_{\rm m}h \sim 0.15$–$0.25$ and the OCDM model with $\Omega_{\rm m}h \sim 0.25$–$0.35$. Perhaps promising results can also be reached for MDM models with similar parameters.

(v) A large-scale bias between the spatial distribution of DM and galaxies can increase the galaxy concentration within RSE by a factor of about 2 which essentially improves the simulated characteristics of RSE. The technique used above allows us to reveal reliably the influence of the biasing and to discriminate between bias models.

(vi) The simulated parameters of DM structure are consistent with the theoretical expectations. The main cosmological parameters can be successfully reconstructed using the measured properties of the large-scale matter distribution. After correcting for the bias and for selections effects, these methods can be applied to observed galaxy catalogues.

(vii) Our results verify also the theoretical expectations with respect to the epoch of the RSE formation. At $z = 1$ the fraction of matter accumulated by RSE with the chosen richness and overdensity drops by a factor ∼2, and at $z = 3$ it becomes negligible.

The main statistical characteristics of the RSE are listed in Tables 2–5 in comparison with the properties found for the observed galaxy distribution. These results verify the existence of a wall-like component with similar characteristics in both observations and simulations performed for suitable models. A similar range of cosmological models was recently separated by Cole et al. (1997) and by Bahcall & Fan (1998) from a comparison of observed and simulated properties of clusters of galaxies. The observations of supernovae at high redshifts (Perlmutter et al. 1998) are more consistent with the ΛCDM model with $\Omega_{\rm m} \sim 0.3$.

Currently, there is some observational evidence of large matter inhomogeneities at redshifts $z \sim 0.5$–1 and higher (Williger at al. 1996; Cristiani et al. 1996; Quashnock, Vanden Berk & York 1996, 1998; Connolly et al. 1996). Our analysis shows that for the models considered, these structures cannot be as common as at small redshifts. A more detailed statistical description of the absorption spectra of quasars is required to obtain the characteristics of structures at high redshifts.

At small redshifts further progress in investigations of observed large-scale matter distribution is linked with very large galaxy redshift catalogues as the 2dF redshift survey of 250,000 galaxies (Colless 1999) and the million galaxy Sloan Digital Sky Survey (Loveday & Pier 1998). The available surveys used above for the comparison with simulated structure parameters (the Durham/UKST Galaxy Redshift Survey, Ratcliffe et al. 1996; and the Las Campanas Redshift Survey, Shectman et al. 1996) are not so representative and moreover they are limited in use to specific selection effects (see discussion in Sections 6.1 and 6.3). In spite of this, now and within the next few years results obtained with these surveys provide us with the best characteristics of observed large-scale matter distribution.

9.2 Remarks about the method

The study of simulations is currently the best way for understanding the large-scale matter distribution. The large boxes used for simulations allow us to obtain a representative description of large-scale perturbations and their mutual interactions with perturbations on smaller scales, as well as to obtain a representative statistic of RSE. Both factors are equally important for the successful reproduction of the matter distribution observed in large galaxy surveys.

The analysis of six simulations performed by Madsen et al. (1998) shows that simulations reproduce the theoretical distributions only on the scales ~ 0.1–$0.15)L_{\rm box}$. This means that realistic

simulations of the observed large-scale matter distribution are possible for $L_{\rm box} \geq (400-500)\,h^{-1}$ Mpc, whereas for smaller box sizes random variations of parameters of large-scale structure are expected.

The analysis was performed mainly for rectangular slices with the size $(500\times500\times50)\,h^{-3}$ Mpc^3 which accumulate about 10 per cent of the particles. Such an approach allows us to study a broad set of cosmological models with a reasonable precision and representativity. To test the possible impact of the selection used, the analysis was repeated for the full simulated sample of the ΛCDM model in comoving coordinates. The results are consistent with what was found above, and the difference is less than 10 per cent. The comparison of results obtained for two ΛCDM models also shows the difference between the structure parameters and the velocity dispersions ∼10 per cent. Variations of $\sigma_{\rm vel}$ and σ_8 listed in Table 1 are also ∼10 per cent. These results characterize the actual precision reached in the investigation, and show that even for large boxes the main structure parameters are moderately sensitive to the random realization.

The comparison of the data presented with data of a similar simulation (Cole et al. 1997) performed with higher resolution (P3M code) demonstrates the moderate dependence of the main simulated structure parameters on these factors. The properties of high-density clumps are sensitive to the resolution that distorts the FDMST for smaller lengths (in comoving space). These distortions, however, disappear in redshift space. The same factor increases the simulated velocity dispersion. The main quantitative characteristics of the RSE are nonetheless sufficiently stable.

ACKNOWLEDGMENTS

We are grateful to our anonymous referee and M.Demiański for the very useful comments and criticism. This paper was supported in part by Denmark's Grundforskningsfond through its support for the establishment of the Theoretical Astrophysics Center and grant INTAS-93-68. AGD and VIT also acknowledge support from the Center of Cosmo-Particle Physics, Moscow.

REFERENCES

Amendola L., Gottlöber S., Mücket J. P., Müller V., 1995, ApJ, 457, 444
Babul A., Starkman G. D., 1992, ApJ, 401, 28
Bahcall N. A., Fan X., 1998, ApJ, 504, 1
Bardeen J. M., Bond J. R., Kaiser N., Szalay A., 1986, ApJ, 304, 15 (BBKS)
Barrow J., Bhavsar S., Sonoda D., 1985, MNRAS, 216, 17
Bellanger C., de Lapparent V., 1995, ApJ, 455, L103
Broadhurst T. J., Ellis R. S., Koo D. C., Szalay A. S., 1990, Nat, 343, 726
Bunn E. F., White M., 1997, ApJ, 480, 6
Bunn E. F., Scott D., White M., 1995, ApJ, 441, L9
Buryak O. E., Doroshkevich A. G., Fong R., 1994, ApJ, 434, 24
Cohen J. G., Hogg D. W., Pahre M. A., Blandford R., 1996, ApJ, 462, L9
Cole S., Weinberg D. H., Frenk C. S., Ratra B., 1997, MNRAS, 289, 37
Cole S., Hatton S., Weinberg D. H., Frenk C. S., 1998, MNRAS, 300, 945
Coles P., 1993, MNRAS, **262**, 1065
Colless M. M., 1999, Phil. Trans. R. Soc. London A, 357, 105
Connolly A. J., Szalay A. S., Koo D., Romer A. K., Holden B., Nichol R. C., Miyaji T., 1996, ApJ, 473, L67
Cristiani S., D'Odorico S., D'Odorico V., Fontana A., Giallongo E., Savaglio S., 1996, MNRAS, 285, 209
de Lapparent V., Geller M. J., Huchra J. P., 1988, ApJ, 332, 44
Dekel A., 1997, in DaCosta L. N., Renzini A., eds., Galaxy Scaling, Relations: Origins, Evolution and Applications. Springer, Berlin, p. 245
Dekel A., Rees M. J., 1987, Nat, 326, 455
Dekel A., Silk J., 1986, ApJ, 303, 39
Demiański M., Doroshkevich A., 1999c, in Proc. Eighth Marcel Grossmann Meeting on General Relativity, in press
Demiański M., Doroshkevich A., 1999a, ApJ, 512, 527
Demiański M., Doroshkevich A., 1999b, MNRAS, in press, (astro-ph/9901400)
Demiański M., Doroshkevich A., 1999c, in Piran T., ed., The Eighth Marcel Grossmann Meeting. World Scientific, Singapore, in press
Doroshkevich A., 1980, AZh, 57, 259
Doroshkevich A. G., Tucker D. L., Oemler A., Kirshner R. P., Lin H., Shectman S. A., Landy S. D., Fong R., 1996, MNRAS, 283, 1281 (LCRS1)
Doroshkevich A. G., Fong R., Gottlöber S., Mücket J. P., Müller V., 1997a, MNRAS, 284, 633
Doroshkevich A. G.,Tucker D. L., Lin H., Turchaninov V., Fong R., 1997b, preprint TAC 1997-031 MNRAS, submitted (LCRS2)
Doroshkevich A., Gottlöber S., Madsen S., 1997c, A&AS, 123, 495
Doroshkevich A. G., Fong R., Tucker D., Turchaninov V., 1998a, in Olinto A., Frieman J., Schramm D., eds, Proc. 18th Texas Symposium on Relativistic Astrophysics and Cosmology. World Scientific, Singapore, p. 560
Doroshkevich A., Fong R., Makarova O., 1998b, A&A, 329, 14
Doroshkevich A, Fong R., McCracken H., Ratcliff A., Shanks T., Turchaninov V. I., 1999, MNRAS, submitted.
Dressler A., Faber S. M., Burstein D., Davies R. L., Lynden-Bell D., Terlevich R. J., Wegner G., 1987, ApJ, 313, L37
Ghigna S., Bonometto S. A., Retzlaff J., Gottlöber S., Murante S., 1996, ApJ, 469, 40
Giovanelli R., Haynes M. P., 1993, AJ, 105, 1271
Gottlöber S., Müller V, Starobinsky A. A., 1991, Phys. Rev. D, 43, 2510
Gottlöber S., Mücket J. P., Starobinsky A. A., 1994, ApJ, 434, 417
Kates R., Müller V., Gottlöber S., Mücket J. P., Retzlaff J., 1995, MNRAS, 277, 1254
Kirshner R. P., Oemler A. J., Schechter P. L., Shectman S. A., 1983, AJ, 88, 1285
Klypin A. A., Shandarin S. F., 1993 ApJ, 413, 48
Lin H., Kirshner R. P., Shectman S. A.,Landy S. D., Oemler A., Tucker D. L., Schechter P. L., 1996, ApJ, 464, 60
Loveday J., Pier J., 1998, in Colombi S., Mellier Y., Raban B., eds, Proc. 14th IAP Astrophysics Colloq., Wide Field Surveys in Cosmology. Editions Frontieres, Gif-sur-Yvette, p. 317
Lucchin F., Matarrese S., 1985, Phys. Rev. D, 32, 1316
Madsen S., Doroshkevich A., Gottlöber S., Müller V., 1998, A&A, 329, 1
Morris S. L., Weymann R. J., Dressler A., McCarthy P. J., Smith B. A., Terrile R. J., Giovanelli R., Irwin M., 1993, ApJ, 419, 524
Oort J. H., 1983a, ARA&A, 21, 373
Oort J. H., 1983b, A&A, 139, 211
Ostriker J. P., 1993, ARA&A, 31, 689
Perlmutter S. et al., 1999, ApJ, in press (astro-ph/9812133)
Quashnock J. M., Vanden Berk D. E., York D. G., 1996, ApJ, 472, L69
Quashnock J. M., Vanden Berk D. E., York D. G., 1998, in Olinto A., Frieman J., Schramm D., eds, Eighteenth Texas Symposium on Relativistic Astrophysics and Cosmology. World Scientific, Singapore, p. 655
Ramella M., Geller M. J., Huchra J. P., 1992, ApJ, 384, 396
Ratcliffe A., Shanks T., Broadbent A., Parker Q. A., Watson F. G., Oates A. P., Fong R., Collins C. A., 1996, MNRAS, 281, L47
Retzlaff J. Borgani S., Gottlöber S., Klypin A., Müller V., 1998, New Astron., 3, 631
Sahni, V., Coles, P., 1995, Phys. Rep., 262, 1
Sahni V., Sathyaprakash B. S., Shandarin S. F., 1994, ApJ, 431, 20
Sathyaprakash B. S., Sahni V., Shandarin S. F., 1998, ApJ, 508, 551
Schramm D. N., 1998 in Olinto A., Frieman J., Schramm D., eds, Eighteenth Texas Symposium on Relativistic Astrophysics and Cosmology. World Scientific, Singapore, p. 1
Shandarin S., Zel'dovich Ya. B., 1989, Rev. Mod. Phys., 61, 185
Shectman S. A. et al., 1996, ApJ, 470, 172
Shull J. M., Stocke J. T., Penton S. V., 1996, AJ, 111, 72
Stocke J. T., Shull J. M., Penton S., Donahue M., Carilli C., 1995, ApJ, 451, 24

Tucker D. et al., 1997, MNRAS, 285, L5
Valinia A., Shapiro P. R., Martel, H., Vishniac E. T., 1997, ApJ, 479, 46
van de Weygaert R., 1991, PhD thesis, Univ. Leiden
Vishniac E. T., 1983, ApJ, 274, 152
Vishniac E. T., 1986, in Kolb E. W., Turner M. S., Lindley D., Olive K., Seckel D., eds, Inner Space/Outer Space. U. Chicago Press, Chicago, p. 190
Weistrop D., Hintzen P., Kennicutt R. C., Liu C., Lowenthal J., Cheng K. P., Oliversen R., Woodgate B., 1992, ApJ, 396, L23
White S. D. M., Briel U. G., Henry J. P., 1993, MNRAS, 261, L8
Williger G. M., Hazard C., Baldwin J. A., McMahon R. G., 1996, ApJS, 104, 145
Willmer C. N. A., Koo D. C., Szalay A. S., Kurtz M. J., 1994, ApJ, 437, 560
Zel'dovich Ya. B., 1970, A&A, 5, 20
Zel'dovich Ya. B., 1978, in Longair M., Einasto J., eds, Large Scale Structure in the Universe. Reidel, Dordrecht, p. 409

This paper has been typeset from a TEX/LATEX file prepared by the author.